MJO Simulation Diagnostics

CLIVAR MADDEN–JULIAN OSCILLATION WORKING GROUP:

D. WALISER,* *Jet Propulsion Laboratory, Pasadena, California;* K. SPERBER,* *Lawrence Livermore National Laboratory, PCMDI, Livermore, California;* H. HENDON, *Centre for Australian Weather and Climate Research, Melbourne, Australia;* D. KIM, *Seoul National University, Seoul, Korea;* E. MALONEY, *Colorado State University, Fort Collins, Colorado;* M. WHEELER, *Centre for Australian Weather and Climate Research, Melbourne, Australia;* K. WEICKMANN, *NOAA/Earth System Research Laboratory, Boulder, Colorado;* C. ZHANG, *Rosenstiel School of Marine and Atmospheric Science, Miami, Florida;* L. DONNER, *NOAA/GFDL, Princeton, New Jersey;* J. GOTTSCHALCK, *NOAA/NCEP, Camp Springs, Maryland;* W. HIGGINS, *NOAA/NCEP, Camp Springs, Maryland;* I.-S. KANG, *Seoul National University, Seoul, Korea;* D. LEGLER, *U.S. CLIVAR Office, Washington, D.C.;* M. MONCRIEFF, *NCAR, Boulder, Colorado;* S. SCHUBERT, *NASA/GSFC, Greenbelt, Maryland;* W. STERN, *NOAA/GFDL, Princeton, New Jersey;* F. VITART, *European Centre for Medium-Range Weather Forecasts, Reading, United Kingdom;* B. WANG, *IPRC, University of Hawaii, Honolulu, Hawaii;* W. WANG, *NOAA/NCEP, Camp Springs, Maryland;* S. WOOLNOUGH, *University of Reading, Reading, United Kingdom*

(Manuscript received 17 July 2008, in final form 13 November 2008)

ABSTRACT

The Madden–Julian oscillation (MJO) interacts with and influences a wide range of weather and climate phenomena (e.g., monsoons, ENSO, tropical storms, midlatitude weather), and represents an important, and as yet unexploited, source of predictability at the subseasonal time scale. Despite the important role of the MJO in our climate and weather systems, current global circulation models (GCMs) exhibit considerable shortcomings in representing this phenomenon. These shortcomings have been documented in a number of multimodel comparison studies over the last decade. However, diagnosis of model performance has been challenging, and model progress has been difficult to track, because of the lack of a coherent and standardized set of MJO diagnostics. One of the chief objectives of the U.S. Climate Variability and Predictability (CLIVAR) MJO Working Group is the development of observation-based diagnostics for objectively evaluating global model simulations of the MJO in a consistent framework. Motivation for this activity is reviewed, and the intent and justification for a set of diagnostics is provided, along with specification for their calculation, and illustrations of their application. The diagnostics range from relatively simple analyses of variance and correlation, to more sophisticated space–time spectral and empirical orthogonal function analyses. These diagnostic techniques are used to detect MJO signals, to construct composite life cycles, to identify associations of MJO activity with the mean state, and to describe interannual variability of the MJO.

1. Introduction

The Madden–Julian oscillation (Madden and Julian 1971, 2005) is the dominant component of intraseasonal variability in the tropical atmosphere. It is characterized by eastward-propagating, equatorially trapped, baroclinic oscillations in the tropical wind field. During a typical MJO event, a positive convection/rainfall anomaly develops over the western Indian Ocean, while convection tends to be suppressed further east over the western Pacific. Over the course of the following 40–50 days, the enhanced convective anomaly in the Indian Ocean intensifies and propagates slowly eastward (3–5 m s^{-1}) to the central Pacific Ocean. The convection anomalies associated with the MJO are most intense over the central/eastern Indian Ocean and western Pacific Ocean, and they often diminish over the Maritime Continent. Over the warmer tropical waters in the Eastern Hemisphere, the MJO exhibits large-scale convection anomalies that interact strongly with the tropospheric circulation and surface fluxes of mass, heat, and momentum. Once the disturbances reach the date line, and thus cooler equatorial waters, convection subsides and the disturbance is largely confined to dynamical fields (Rui and Wang 1990; Hendon and Salby 1994;

---

* Co-chairs.

Corresponding author address: Duane Waliser, Jet Propulsion Laboratory, MS 183-505, California Institute of Technology, 4800 Oak Grove Drive, Pasadena, CA 91109.
E-mail: duane.waliser@jpl.nasa.gov

DOI: 10.1175/2008JCLI2731.1

Matthews 2000; Sperber 2003; Kiladis et al. 2005). These characteristics, especially the eastward propagation along the equator, tend to be most strongly exhibited during boreal winter (November–April), when the Indo-Pacific warm pool is centered near the equator. During boreal summer (May–October), the asymmetry of the mean state associated with the Asian summer monsoon tends to result in northeastward propagation of the convection/circulation anomalies from the equatorial Indian Ocean into Southeast Asia, while at the same time exhibiting eastward propagation along the equator (Yasunari 1981; Wang and Rui 1990; Annamalai and Sperber 2005; Waliser 2006). This eastward propagation of the boreal summer MJO is associated with significant impacts in the east Pacific warm pool and North American monsoon system (Maloney and Esbensen 2003; Barlow and Salstein 2006; Lorenz and Hartmann 2006), and in sub-Saharan Africa (Matthews 2004; Maloney and Shaman 2008). More comprehensive reviews of the MJO can be found in Madden and Julian (1994), Lau and Waliser (2005), and Zhang (2005).

Interest in the MJO has intensified in recent years (Zhang et al. 2001; Schubert et al. 2002; Waliser et al. 2003c; ECMWF 2004; ICTP 2006) because of its extensive interactions with other components of the climate system and because it represents a connection between the weather and seasonal-to-interannual climate variations. For example, the distinctive onsets and breaks of the Asian–Australian monsoon are closely related to MJO activity (e.g., Yasunari 1980; Hendon and Liebmann 1990; Goswami 2005; Wheeler and McBride 2005; Straub et al. 2006). Thus it is implied that our understanding and ability to predict the MJO and the Asian–Australian monsoon are critically linked (e.g., Webster et al. 1998; Waliser et al. 1999a; Sperber et al. 2001; Waliser et al. 2003d; Webster and Hoyos 2004). Eastward-propagating MJO convective activity can at times modulate the timing and evolution of El Niño because of its close connection with near-surface zonal wind activity in the Pacific (Lau and Chan 1988; Lau and Shen 1988; Weickmann 1991; Takayabu et al. 1999; Kessler and Kleeman 2000; Bergman et al. 2001; Zhang and Gottschalck 2002; Kessler 2005; Lau 2005; Straub et al. 2006; Hendon et al. 2007). Many studies have shown an influence of the MJO on the character and strength of higher frequency tropical variability, including the diurnal cycle (Chen et al. 1996; Tian et al. 2006), tropical cyclones (Nakazawa 1986; Liebmann et al. 1994; Higgins et al. 2000; Maloney and Hartmann 2000a; Bessafi and Wheeler 2006; Frank and Roundy 2006), and extreme precipitation events (Mo and Higgins 1998; Jones 2000; Jones et al. 2004a). The MJO's influence extends, via teleconnection mechanisms, to the extratropical circulation and its weather patterns (Weickmann 1983; Liebmann and Hartmann 1984; Higgins and Mo 1997; Vecchi and Bond 2004; Weickmann and Berry 2006). This suggests that medium- and long-range midlatitude weather forecasts by global models would benefit from accurate prediction of the MJO (Ferranti et al. 1990; Hendon et al. 2000; Whitaker and Weickmann 2001; Jones et al. 2004b). Finally, recent studies have also shown strong MJO influences on biological and chemical components of our climate system (Waliser et al. 2005; Tian et al. 2008, 2007; Wong and Dessler 2007). While this list of interactions associated with the MJO is continuing to grow, the brief itemization above indicates the MJO to be neither a benign weather pattern nor just a semicoherent form of climate ''noise'' but rather a phenomenon we must understand and correctly represent in our global weather/climate models.

As important as the MJO is in our weather/climate system, we still struggle to represent it correctly in our global climate simulations (Slingo et al. 2005) and we have yet to exploit it in our numerical weather or subseasonal-climate forecasts (Schubert et al. 2002; Newman et al. 2003; Seo et al. 2005; Waliser 2005; Woolnough et al. 2007). A survey of the multimodel assessments that have been made over the last decade of the capabilities of GCMs to represent the MJO shows progress to be slow (Slingo et al. 1996; Sperber et al. 2000; Waliser et al. 2003a; Lin et al. 2006; Zhang et al. 2006), and that we have yet to develop a single GCM that the climate modeling community would agree has a ''good'' MJO when scrutinized in some detail and that has been maintained through GCM revisions/updates. The inability of models to simulate the MJO has long been thought to relate to deficiencies in the treatment of cumulus convection. This is because typically the greatest sensitivity that the MJO simulation exhibits to various model ''tunings'' is associated with that of the convective parameterization—or closely related processes such as cloud–radiative feedbacks (e.g., Slingo et al. 1996; Wang and Schlesinger 1999; Lee et al. 2001; Maloney and Hartmann 2001; Maloney 2002; Lee et al. 2003). Related to the issues of convective parameterization are the confounding issues concerning the representation of the basic state, including a preference for overdoing the ''double ITCZ'' (Lin 2007), a poor mean rainfall structure in the Indian Ocean (Sperber and Annamalai 2008), equatorial surface westerly winds that are too weak or too limited in their zonal extent (Inness and Slingo 2003), uncertainty in the importance of ocean–atmospheric coupling (e.g., Gualdi et al. 1999a; Waliser et al. 1999b; Hendon 2000; Kemball-Cook et al. 2002; Inness et al. 2003; Zheng et al. 2004; Sperber et al. 2005; Zhang et al. 2006), the importance of achieving a proper phasing and representation of surface fluxes (e.g., Shinoda et al. 1998; Woolnough et al. 2000; Maloney and Sobel 2004), and the importance of ocean mixed-layer processes (e.g., Shinoda and Hendon 1998; Waliser et al. 2003b; Bernie et al. 2005).

One of the chief difficulties in evaluating success and tracking improvement in our GCM simulations of the MJO is the lack of a consistent set of diagnostics. Somewhat remarkable is the fact that of the five multimodel MJO evaluations mentioned above, with the exception of seasonal mean precipitation maps, not a single diagnostic is applied in the same manner in even two of the studies. The diagnostics most similar among these studies are simple measures of intraseasonal precipitation variance. Even in this case, the filtering and/or plotting (e.g., map versus latitude average) are performed differently. A robust set of observation-based diagnostics is needed to better gauge our progress in simulating the MJO, make comparisons among models, and make inroads at diagnosing the shortcomings in physical parameterization underlying our inadequate MJO simulations.

To help address this need, U.S. CLIVAR established the MJO Working Group (MJOWG) in the spring of 2006 (more information available online at http://www.usclivar.org/Organization/MJO_WG.html). Chief among this working group's objectives was the development of observation-based diagnostics that allow a more consistent, and hopefully insightful, assessment of model performance regarding the MJO. Over the course of the following year, this working group developed these diagnostics via teleconferences and meetings during the U.S. CLIVAR Summit in July 2006 as well as informally at a number of scientific meetings and workshops. The group considered issues such as ease of use versus level of physical insight, potential pitfalls/ambiguity in the interpretation of the model-data comparisons, observation quality, availability, and sensitivity. In the development process, observations were used to assess the sensitivity to stratifying the analysis by season, the size of analysis domain, the need (or lack thereof) for using tapering or detrending during spectral analysis, the method for assessing statistical significance, etc.

This paper describes the outcome of the above effort; specifically it describes the diagnostics developed by the U.S. CLIVAR MJOWG for assessing the ability of climate models to simulate the boreal winter Madden–Julian oscillation and its boreal summer counterpart. For brevity, the term MJO is used throughout this article, and it includes the broader category of eastward and northward tropical intraseasonal oscillations that occur on time scales of 30–70 days. The diagnostics have been categorized into two levels of increasing complexity. Level 1 diagnostics are meant to provide a basic indication of model spatial and temporal intraseasonal variability that can be easily understood and calculated by the non-MJO expert. Ease of use dictated that the analytic procedures be as simple and uniform as possible for summer and winter calculations. Level 2 diagnostics provide a more comprehensive diagnosis of the MJO through multivariate analysis, wavenumber-frequency spectral decomposition, and composite analysis of the MJO life cycle. In addition to the level 1 and level 2 diagnostics, additional diagnostics include aspects of the mean state found to be relevant to MJO simulation fidelity and a characterization of MJO interannual variability. The primary variables used for level 1 and 2 diagnostics are: outgoing longwave radiation (OLR), precipitation, and zonal wind at 850 and 200 hPa. However, a number of other variables are included in life cycle composites and mean field descriptions.

With the publication of these diagnostics, we encourage the modeling and diagnostic communities to make use of them in studies of the MJO in their models, particularly in terms of presentations at workshops, conferences, and in journal articles. As of this writing, a link to plots of the diagnostics, as well as the code and input data used to generate them, can be found at the MJOWG Web site (http://climate.snu.ac.kr/mjo_diagnostics/index.htm). It is hoped that this more common set of measures will facilitate model assessment and improve the ability to gauge model successes and failures. Together, we hope that these diagnostics will enhance the ability to focus on the underlying physical shortcomings of models by removing some of the burden on individual researchers to decide on, compute, and apply model MJO diagnostics. Section 2 discusses the observations utilized for the diagnostics. Section 3 then provides a description of a subset of the selected diagnostics and how they are calculated, and some motivation for these choices. Finally, section 4 provides a summary, including recommendations for future activities and areas of focus.

2. Observations

We employ observational data that covers most important aspects of the MJO. Where possible, we use multiple datasets from at least two sources in order to account for observational uncertainties. Outgoing longwave radiation, which is a primary source of information on the convective behavior of the MJO, is from the advanced very high resolution radiometer (AVHRR) estimates of Liebmann and Smith (1996).

Three precipitation products are used for this study that are all based, at least in part, on infrared (IR)-based satellite retrievals, and are blended with or adjusted by rain gauge data, other satellite estimates and model prediction data; this provides plenty of spatial/temporal samples but with significant biases. The Climate Prediction Center (CPC) Merged Analysis of Precipitation (CMAP) dataset (Xie and Arkin 1997) first merges IR-based Geostationary Operational Environmental Satellite (*GOES*) Precipitation Index (GPI; Arkin and Meisner 1987) with two kinds of microwave (MW) satellite estimates and model predictions. This output is further blended with gauge-based analysis. To extend the length of the dataset, OLR-based precipitation index (Xie and Arkin 1997) and Microwave Sounding Unit (MSU)-based (Spencer 1993) estimates are used in the period when GPI is not available; that is, before year 1986. As a result, pentad CMAP dataset is available from 1979 to present, of which we used 27 yr (1979–2005).

Unlike CMAP, the second and third precipitation products are daily sampled datasets with shorter length. The Global Precipitation Climatology Project (GPCP; 1997–2005) dataset (Huffman et al. 2001) calibrates GPI data using Special Sensor Microwave Imager (SSM/I) microwave estimates. Our third rainfall product is the 3B42 dataset from the Tropical Rainfall Measuring Mission (TRMM). The algorithm for 3B42 adjusts objectively the rain rates inferred from IR satellite estimates using other TRMM products (Kummerow et al. 2000). The TRMM product used here is not combined with gauge analyses, unlike the first two datasets.

Upper- (200 hPa) and lower- (850 hPa) tropospheric zonal winds are obtained from three global reanalysis products. Two of them are different versions of the National Centers for Environmental Prediction/National Center for Atmospheric Research (NCEP/NCAR) reanalysis (Kalnay et al. 1996) and NCAR–Department of Energy (DOE) Second Atmospheric Model Intercomparison Project (AMIP-II) reanalysis (Kanamitsu et al. 2002). The latter uses improved model physics and has several corrections to the known errors in the former. The European Centre for Medium-Range Weather Forecasts (ECMWF) 40-Year Reanalysis (ERA40; Uppala et al. 2005) is also used. The data period for two NCEP–NCAR reanalyses is 1979–2005 while that for ERA40 is 1979–2001.

For SST two datasets are used, the Optimal Interpolation SST (OISST; Reynolds et al. 2007) and the TRMM microwave imager (TMI) SST (Wentz et al. 2000). OISST is an optimally interpolated SST using AVHRR infrared satellite data with large-scale adjustment of satellite biases with respect to the in situ data (Reynolds et al. 2007). TMI SST uses microwave channels, which are less affected by cloud and aerosols (but significantly affected by raindrops; Wentz et al. 2000). Both the products provide relatively higher spatial resolution (0.25° × 0.25°) and they are gridded into 1.0° × 1.0° (OISST) and 2.5° × 2.5° (TMI) grid resolution, respectively. We use the coarser resolution version of TMI to minimize the impact of missing values in daily maps.

Latent heat flux is obtained from the two reanalyses—NCEP/NCAR reanalysis and ERA40 and from the Objectively Analyzed Air–Sea Fluxes (OAFlux) for the global ice-free oceans (Yu and Weller 2007). Net surface shortwave radiation data are obtained from the Global Energy and Water Cycle Experiment (GEWEX) Surface Radiation Budget (SRB) products (Gupta et al. 2001) and the International Satellite Cloud Climatology Project (ISCCP) datasets (Zhang et al. 2004). Independent variables in bulk aerodynamic formula for surface latent heat flux (e.g., surface wind speed, specific humidity) are obtained through synthesizing several satellite retrievals and two reanalyses in OAFlux (Yu and Weller 2007). The error properties of both input data in OA procedure are obtained using Comprehensive Ocean–Atmosphere Dataset (COADS) (Woodruff et al. 1998) ship observations as the base data. To derive surface shortwave radiative flux, different algorithms are used in GEWEX-SRB (Langley Parameterized Shortwave Algorithm; LPSA) and ISCCP-FD (GISS GCM radiative transfer model) but they share input sources of cloud properties (ISCCP-DX), surface albedo [Earth Radiation Budget Experiment (ERBE)] and column ozone [Total Ozone Mapping Spectrometer (TOMS)].

Tables 1, 3, and 4 indicate the specific application of the observations discussed above, and the right columns list the abbreviations that will be used in this paper to represent the datasets. Daily averages, except for CMAP, which is pentad based, are used for level 1 and level 2 diagnostics while mean state diagnostics are calculated using monthly means. The period used for the calculations shown in all the figures is 27 yr (1979–2005; with the exception of the OISST in Figs. 13 and 14, which is 4 January 1985–31 December 2005).

3. Diagnostics

This section presents select examples of the diagnostics developed by the MJOWG. Given space limitations, the diagnostics presented here are by no means exhaustive, though they might be considered to be the most basic and informative and thus are a good starting point for an analysis of the MJO. The complete set of diagnostics is provided at the MJOWG Web site (http://climate.snu.ac.kr/mjo_diagnostics/index.htm), and is also

TABLE 1. Level 1 diagnostics.

Diagnostic	Season	Regions	Fields
Variance (unfiltered, intraseasonal, % of unfiltered)	Boreal summer, winter, all seasons	30°N–30°S, 0°–360°E	OLR, precipitation, U200, U850
Time spectra	Boreal summer, winter, all-seasons	West Pacific, Indian Ocean, east Pacific, Maritime Continent (see Table 2)	OLR, precipitation, U200, U850
Lag–longitude correlation analysis (Indian Ocean reference point using same season and variable-dependent locations as defined in Table 2)	Boreal summer, winter	Equatorial (10°N–10°S averaged), 0°–360°E	OLR, precipitation, U200, U850
Lag–latitude correlation analysis (Indian and west Pacific reference points using same summertime and variable-dependent locations as defined in Table 2)	Boreal summer	Indian: 40°N–40°S, 80°–100°E averaged; west Pacific: 40°N–40°S, 115°–135°E averaged	OLR, precipitation, U200, U850
Single variable EOF analysis (including lag correlation between leading PCs, time spectra of unfiltered PCs)	Boreal summer, winter	30°N–30°S, 0°–360°E	OLR, precipitation, U200, U850

summarized in the tables that follow. As described in section 2, multiple sources of observation-based data for a given variable were used where possible for the diagnostic calculations, and diagnostics using all of these sources are displayed on the Web site. In the discussion below, the source of the variable displayed (e.g., NCEP1 versus ECMWF, or CMAP versus TRMM) was arbitrary, unless otherwise noted.

a. *Diagnostic strategy*

The diagnostics are partitioned into two levels of complexity, referred to as level 1 and level 2, and they also include a number of supplementary diagnostics. Level 1 diagnostics, summarized in Table 1, are meant to provide a general indication of the spatial and temporal intraseasonal variability that can be easily understood and/or calculated by the non-MJO expert. Ease of use dictates that the analytic procedures be as simple and similar as possible for boreal summer and winter calculations. The level 1 diagnostics include an assessment of intraseasonal and total variance, time series spectral analysis over key spatial domains (Table 2), and univariate empirical orthogonal function (EOF) analysis of bandpass-filtered data. Lag-correlation analysis of bandpass-filtered wind and convective variables is also used to assess both eastward equatorial propagation during both boreal summer and winter, and northward propagation in the Eastern Hemisphere during boreal summer. Variables used in level 1 diagnostics include OLR, precipitation, and zonal wind at 850 and 200 hPa.

Level 2 diagnostics, summarized in Table 3, provide a more comprehensive diagnosis of the MJO through multivariate EOF analysis and wavenumber-frequency decomposition. The multivariate EOF analysis is based on OLR and zonal wind at 850 and 200 hPa (Wheeler and Hendon 2004). The dominant intraseasonal principal components (PCs) from multivariate EOF analysis are used to generate MJO life cycle composites, and coherence squared and phase between the PCs are calculated to determine the fidelity of the eastward propagation. However, a number of other variables are included in life cycle composites. Multiscale interactions are also assessed using cross-spectral analysis (coherence squared and phase) between variables.

In addition to the level 1 and level 2 diagnostics, supplementary analyses are presented of some relevant mean state variables, noted in Table 4. As described in past studies (e.g., Slingo et al. 1996; Hendon 2000; Inness et al. 2003; Waliser et al. 2003a; Sperber et al. 2005; Zhang et al. 2006), the ability of a model to simulate the MJO is intimately related to its ability to simulate the mean climate, especially associated with the spatial distribution of mean convection and surface westerly winds that tend to occur over the warmest SST. The occurrence of the MJO is highly episodic (e.g., Salby and Hendon 1994) with the relationship to interannual variation in SST being rather complex, albeit weak (e.g., Slingo et al. 1996; Hendon et al. 1999; Kessler 2001; Lau 2005; Hendon et al. 2007). Efforts at simulating the character of this relationship have had mixed success (e.g., Slingo et al. 1996; Gualdi et al. 1999b; Waliser et al. 2001), and thus an analysis of interannual variability of MJO activity is also included as a supplementary diagnostic.

For both level 1 and level 2 diagnostics, unfiltered anomalies are computed by subtracting the climatological daily (or pentad where appropriate) mean calculated over all years of the data. Intraseasonal (20–100 day)

TABLE 2. Averaging regions for time series spectra.

Region	OLR	Precipitation	U850	U200
Boreal Winter (November–April)				
Indian	10°S–5°N, 75°–100°E	10°S–5°N, 75°–100°E	1.25°–16.25°S, 68.75°–96.25°E	3.75°–21.25°N, 56.25°–78.75°E
West Pacific	20°–5°S, 160°–185°E	20°–5°S, 160°–185°E	1.25°N–13.75°S, 163.75°–191.25°E	3.75°–21.25°N, 123.75°–151.25°E
Maritime Continent	2.5°–17.5°S, 115°–145°E	2.5°–17.5°S, 115°–145°E		
East Pacific				1.25°N–16.25°S, 256.25°–278.75°E
Boreal summer (May–October)				
Indian	10°S–5°N, 75°–100°E	10°S–5°N, 75°–100°E	21.25°–3.75°N, 68.75°–96.25°E	1.25°N–16.25°S, 43.75°–71.25°E
Bay of Bengal	10°–20°N, 80°–100°E	10°–20°N, 80°–100°E		
West Pacific	10°–25°N, 115°–140°E	10°–25°N, 115°–140°E	3.75°–21.25°N, 118.75°–146.25°E	3.75°–21.25°N, 123.75°–151.25°E
East Pacific			6.25°–16.25°N, 241.25°–266.25°E	1.25°N–16.25°S, 238.75°–266.25°E

bandpass-filtered anomalies are constructed using a 201-point Lanczos filter (Duchon 1979), which has half-power points at 20- and 100-day periods. In addition, the statistical significance of the EOFs that are computed with bandpass-filtered data is assessed by projecting the EOFs back onto the unfiltered anomalies (with only the seasonal cycle removed). Spectral analysis is then conducted on the resulting unfiltered PCs to test the significance of spectral power at intraseasonal time scales against a red noise background using 10% and 5% significance levels (e.g., Maloney and Hartmann 1998). No windowing/tapering or detrending was applied in calculation of these spectra, since sensitivity tests indicated their application had a negligible impact on the results.

We note that in addition to conducting EOF analysis directly on model fields, it also useful to project the model's bandpass-filtered anomalies onto the EOFs of observed variability to assess how well the model simulates the observed MJO. This technique allows direct comparison among all models and the observations and is especially suitable for diagnosis of forecasts of the MJO since the data are projected onto the same observed basis functions. This technique was demonstrated by Duffy et al. (2003) for the NCAR Community Climate Model (CCM3.6), and in Sperber (2004) for the NCAR Community Atmosphere Model (CAM2.0) and Community Climate System Model (CCSM2.0), and Sperber et al. (2005) for numerous ECHAM4-based models, in which the ability to simulate the observed lead–lag relationships between the leading PCs was assessed. The time lag at which the two PCs have a maximum correlation gives the transition time for the MJO convection and/or winds to shift from the Indian Ocean and the western Pacific, with the value of the maximum correlation being a measure of how coherent the convection and/or wind anomalies are between these two regions.

The observed MJO exhibits distinctly different behavior in northern summer and southern summer. Hence, we perform many of our diagnostics for two broadly defined seasons: boreal summer (May–October), and boreal winter (November–April). For some diagnostics, computations are performed for specific domains

TABLE 3. Level 2 diagnostics.

Diagnostic	Season	Regions	Fields
Single variable wavenumber-frequency spectra	Boreal summer, winter, all-season	Equatorial (10°N–10°S averaged), 0°–360°E	OLR, precipitation, U200, U850, Usfc
Wheeler and Kiladis (1999) single variable wavenumber-frequency diagrams	All-season	Equatorial (15°N–15°S averaged), 0°–360°E	OLR, precipitation, U200, U850, Usfc
Cross spectra in the wavenumber-frequency domain (e.g., Hendon and Wheeler 2008)	All-season	Equatorial (15°N–15°S averaged), 0°–360°E	OLR vs U200, U850, Usfc
Mutivariate EOF analysis (including lag correlation between leading PCs, coherence squared, and phase between leading PCs, time spectra of unfiltered PCs)	Boreal summer, winter, all-season	Equatorial (15°N–15°S averaged), 0°–360°E	OLR, U850, U200
MJO life cycle composites: Horizontal	Boreal summer, winter	20°N–20°S, 0°–360°E	OLR, precipitation, U,V200, U,V850, U, Vsfc, SLP, Ψ200, SST, surface LH and SW flux
MJO life cycle composites: Vertical	Boreal summer, winter	0°–360°E, 0 hPa–surface	U, T, q, Ω,

TABLE 4. Supplemental diagnostics.

Diagnostic	Season	Regions	Fields
Mean state analysis: Horizontal	Boreal summer, winter	40°N–40°S, 0°–360°E	Precipitation, SST, U200, U850, Usfc, U200–U850 shear
Mean state analysis: Vertical	Boreal summer, winter	Surface to 0 hPa	U, T, q, Ω
Interannual variability: $\mathrm{PC1}^2 + \mathrm{PC2}^2$ from multivariate EOF analysis	All-season	Equatorial (15°N–15°S averaged), 0°–360°E	OLR, U850, U200
Interannual variability: 91-day running mean of variance averaged over horizontal domain	All-season	10°N–10°S, 0°–360°E10°N–10°S, 40°–180°E	OLR, U850

of interest. These domains are given in the Table 2 and were determined from examination of observed variance maps to isolate regions where observed variance is large.

b. Mean state

Mean fields for 850-hPa zonal wind, rainfall, and SST are presented for boreal summer (Fig. 1) and boreal winter (Fig. 2). As highlighted in section 3a, an analysis of a number of relevant mean fields is a crucial starting point for assessment of both ocean–atmosphere coupled (hereafter, ''coupled'') and atmosphere-only (hereafter, ''uncoupled'') simulations of the MJO. For example, aspects of the convective mean state that are relevant to the MJO include proper latitudinal and zonal locations of the ITCZ, and a realistic simulation of mean lower tropospheric westerly winds, especially their zonal extent across the warm pool of the Indian and west Pacific Oceans. Capturing seasonal variations of the background state is also critical. In uncoupled simulations, convective and westerly wind regions generally coincide with warmest SST. In coupled simulations, reproducing the observed mean SST distribution is often problematic (e.g., Mechoso et al. 1995), and errors in the coupled SST distribution tend to exacerbate any uncoupled atmospheric errors in lower tropospheric zonal winds and precipitation.

c. Level 1 diagnostics

Figures 3 and 4 show maps of intraseasonal variance of 850-hPa zonal wind and CMAP precipitation for boreal summer and boreal winter, respectively. The prominence of the MJO is emphasized by shading of the percent variance accounted for by the 20–100-day band relative to variance filtered with a wider bandwidth.[1] For the CMAP precipitation, which is available as pentads, this percentage is relative to bandpass variance in the 10–180-day band whereas for the zonal wind, which is available daily, this percentage is relative to bandpass variance in the 2–180-day band. Hence, the shaded maxima tend to be higher for precipitation than for zonal wind because the variance in the 20–100-day band is being compared to a smaller total. Aspects of these plots that provide important benchmarks for climate model simulations include the spatial distribution of intraseasonal variance (especially the relative magnitudes of the maxima in the Indian Ocean versus the west Pacific Ocean), the relative minimum in variance in the Maritime Continent, the percent variance accounted for by the intraseasonal band, and the coincidence of 850-hPa wind and precipitation variance centers. A comparison of Figs. 3 and 4 illustrates that tropical intraseasonal variance tends to be concentrated in the summer hemisphere in lower-tropospheric winds and precipitation, with the percentage variance in the intraseasonal (20–100 day) band tending to peak at about 30%–40% for zonal wind and greater than 50% for precipitation (noting the inflated value for precipitation relative to zonal wind due to use of pentad data). We also see that during boreal summer, the intraseasonal variance of precipitation exhibits a number of maxima associated with the land–sea structure around southern Asia (e.g., Waliser et al. 2003a) and another prominent maximum in the east Pacific warm pool (e.g., Maloney et al. 2008). The details associated with these seasonal variations provide an important test for climate model representations of the MJO.

To isolate the fundamental propagating and time-varying nature of the MJO, level 1 diagnostics also include lag–longitude correlation analyses for regions of maximum intraseasonal variance from Figs. 3 and 4 (the areas are defined Table 2). Figure 5 shows lag–longitude diagrams of intraseasonal precipitation (contours) and 850-hPa zonal winds (colors) correlated against precipitation at an Indian Ocean reference point (equator and 90°E) for boreal winter. They also provide diagnosis of other important characteristics of the MJO, including an

---

[1] The large variance near the domain boundary in the winter hemisphere is associated with extratropical intraseasonal variability.

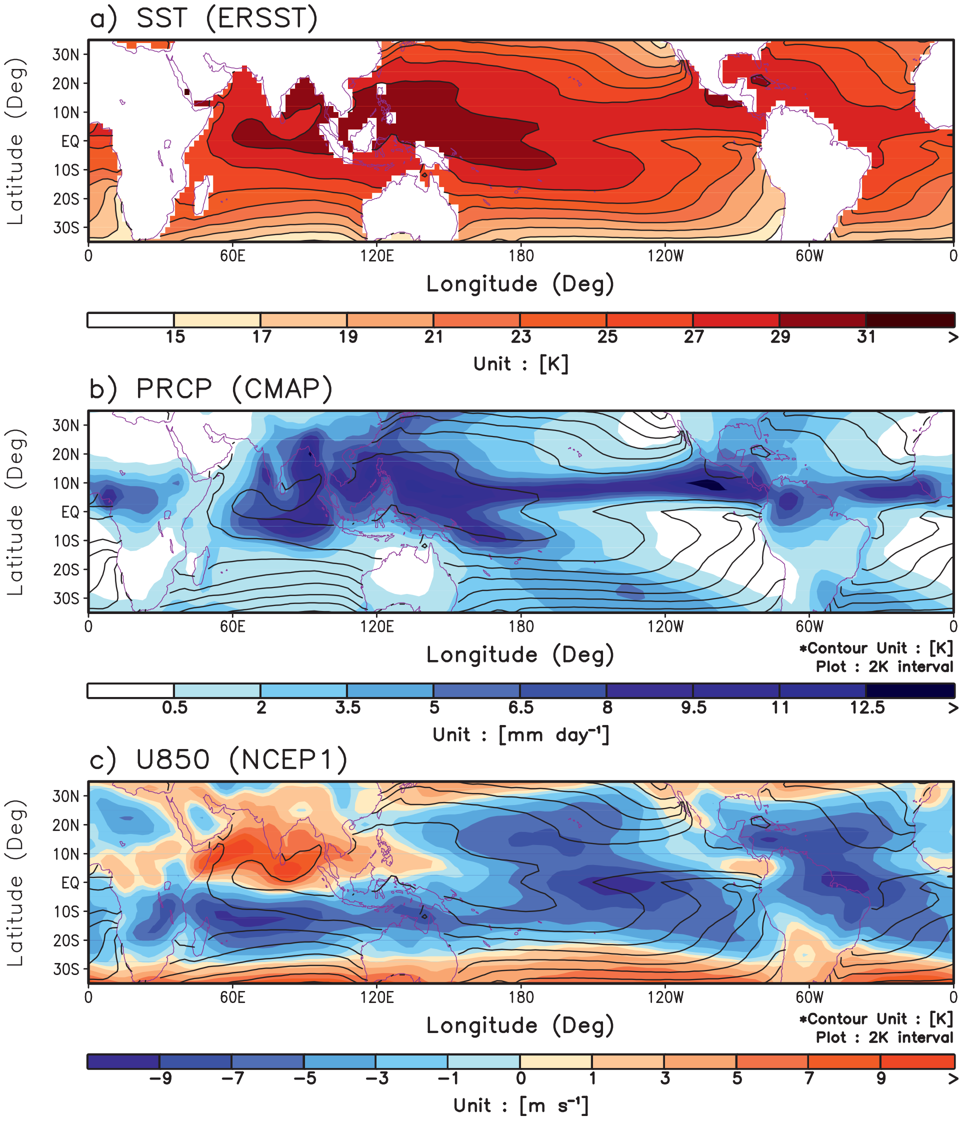

FIG. 1. May–October mean (a) NOAA Extended Reconstructed SST Version 2, (b) CMAP precipitation, and (c) NCEP1 850-hPa zonal wind. The period used in the calculations is 27 yr (1979–2005) unless otherwise specified. Contours of mean SST, plotted every 2 K, are also included in each plot.

estimate of the eastward phase speed across the Eastern Hemisphere of about 4 m s^{-1}, the lag of the zonal wind anomaly behind the precipitation anomaly by about 5–7 days, the confinement of the precipitation anomaly to the Eastern Hemisphere, and the faster eastward propagation of 850-hPa wind in the Western Hemisphere after the decay of precipitation anomaly near the date line. A boreal summer lag–longitude analysis produces qualitatively similar behavior (not shown).

The dominant mode of boreal summer intraseasonal variability is also characterized by distinct northward propagation of intraseasonal anomalies (e.g., Yasunari 1979; Wang and Xie 1997) that occurs in conjunction with the eastward equatorial propagation, thus giving rise to a northwest-to-southeast-tilted rainband (e.g., Annamalai and Sperber 2005). Similar to the lag–longitude diagrams described above to diagnose eastward propagation, lag–latitude plots diagnose northward propagation in the Indian and west Pacific Oceans. In this case, bandpass-filtered fields are averaged over the longitudes of the Indian and west Pacific Ocean reference domains defined in Table 2 for boreal summer, and then regressed against a base point at the equator. Figure 6 shows a boreal summer lag–latitude correlation plot for 850-hPa zonal wind and precipitation averaged over 80°–100°E regressed onto a reference time series of

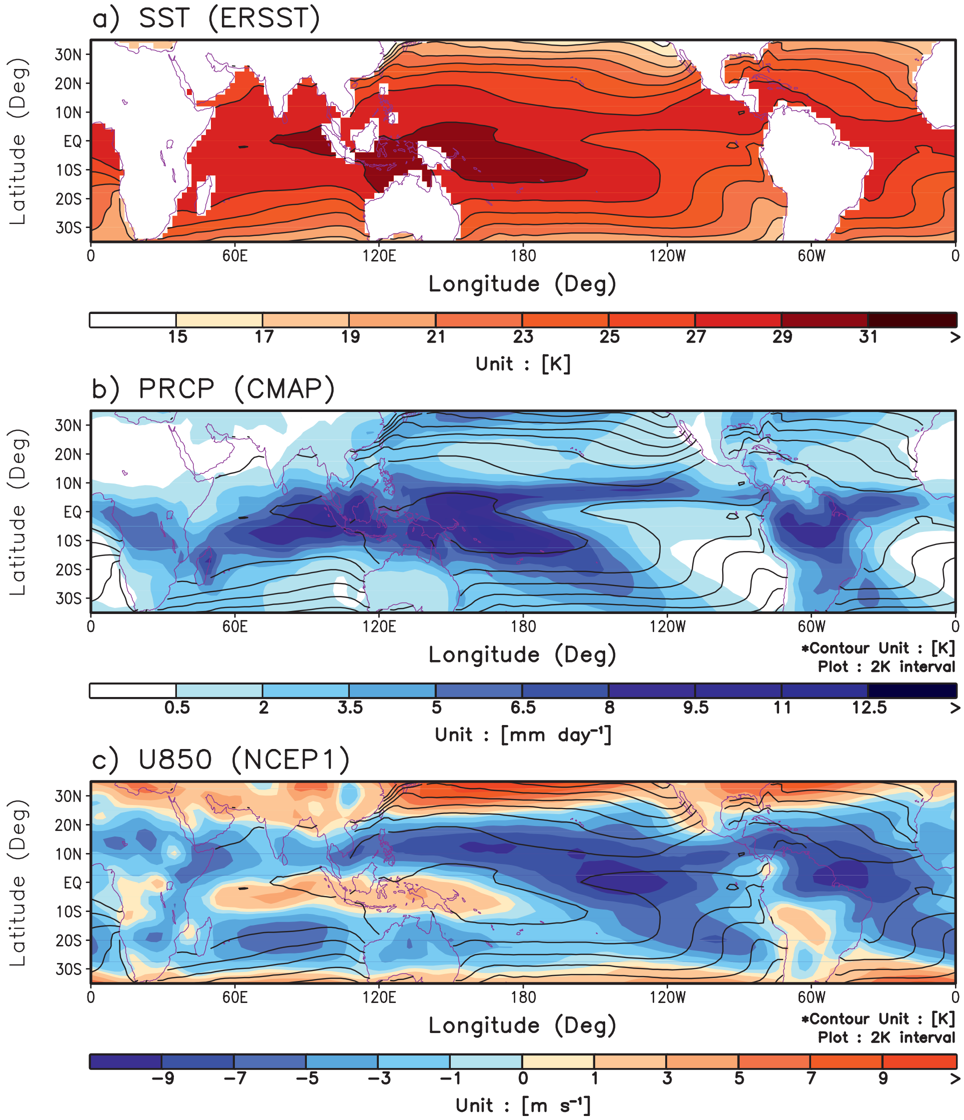

FIG. 2. Same as Fig. 1, except for November–April.

Indian Ocean precipitation. Similar plots are generated for the west Pacific (not shown here). Northward propagation is apparent from the equator into the Northern Hemisphere for both precipitation and zonal wind, with precipitation leading zonal wind by 5–7 days. Interestingly, some evidence of southward propagation from the equator into the Southern Hemisphere is also apparent, which has been reported by Lawrence and Webster (2002) and Annamalai and Sperber (2005).

An additional benefit to a diagnosis such as Fig. 6 is that it implies a propagation speed for intraseasonal anomalies, in this case northward at about 1.2 m s^{-1}. For models it is essential to ascertain if the northward propagation is intimately linked to the near-equatorial eastward propagation (Sperber and Annamalai 2008).

d. Level 2 diagnostics

Level 2 diagnostics are designed to explore more detailed features of the MJO. They include wavenumber-frequency spectra of individual fields, cross-spectral quantities between different fields, and a multivariate EOF analysis. Wavenumber-frequency spectra for equatorial precipitation and 850-hPa zonal wind are shown in Fig. 7 for boreal summer, and in Fig. 8 for boreal winter. The spectra were computed by Fourier transforming 180-day segments centered on boreal summer and boreal winter, forming power, and then averaging over all years of data (1979–2005). The resulting bandwidth is (180 $\text{days})^{-1}$. Only the climatological season cycle was removed before calculation of

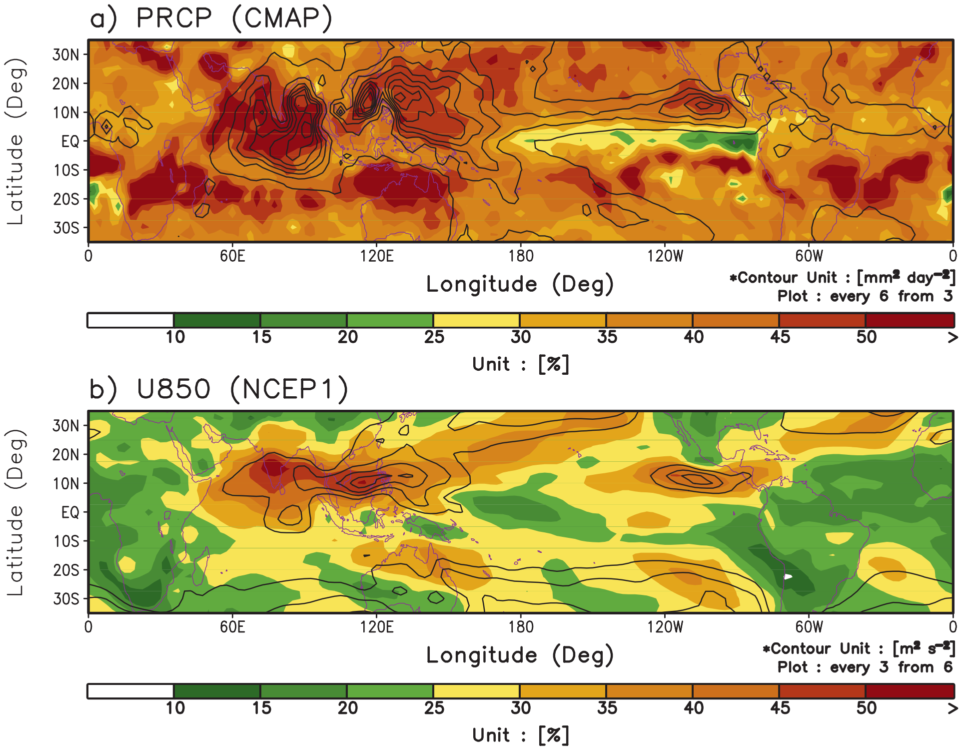

FIG. 3. May–October 20–100-day (a) CMAP precipitation variance and (b) NCEP1 850-hPa zonal wind variance (contours). The percent variance accounted for by the intraseasonal band is shown in color. Contours show intraseasonal variance. Precipitation variance contours are plotted every 6 mm^2 day^{-2}, starting at 3 mm^2 day^{-2}. Zonal wind variance contours are plotted every 3 m^2 s^{-2}, starting at 6 m^2 s^{-2}.

the spectra. By definition, eastward propagation is represented by positive frequency and positive wavenumber whereas westward propagation is represented with one or the other of the frequency or wavenumber being negative. If standing oscillations are present, they will project as equal amounts of power in eastward and westward directions. The results indicate a concentration of power at 30–90-day periods and zonal wavenumber 1 for 850-hPa zonal wind, and zonal wavenumbers 1–3 for precipitation and OLR (e.g., Salby and Hendon 1994). The eastward power is about 4 times that of westward power at intraseasonal frequencies and spatial scales characteristic of the MJO. A comparison between boreal winter and boreal summer spectra indicates that both seasons exhibit qualitatively similar spectral characteristics, although spectral power is reduced slightly at wavenumbers characteristic of the MJO during boreal summer relative to boreal winter. Hence, distinct eastward propagation does occur during boreal summer in both precipitation and winds (e.g., Maloney and Hartmann 2000b; Lawrence and Webster 2002; Wheeler and Hendon 2004). The qualitatively similar spectral behavior during boreal summer and winter also provides justification for the all-season multivariate EOF analysis that is described below and which is used to form the basis of MJO life cycle composites.

In addition to single variable spectral calculations in wavenumber-frequency space, cross-spectral calculations are useful for quantifying the coherence and phase relationships between different variables. Figure 9 shows the coherence squared and phase between equatorial OLR and 850-hPa zonal winds for both symmetric and antisymmetric components of the two fields (Hendon and Wheeler 2008). The symmetric component of a variable F is defined as $F_s(\phi) = [F(\phi) + F(-\phi)]/2$, and the antisymmetric component is defined as $F_a(\phi) = [F(\phi) - F(-\phi)]/2$, where ϕ is latitude (Wheeler and Kiladis 1999). Cross spectra are calculated using data during all seasons on 256-day-long segments, with consecutive segments overlapping by 206 days. Prior to forming coherence squared, the symmetric and antisymmetric powers and cross powers are computed at each symmetric and antisymmetric latitude 0°–10° and then averaged. Colors in Fig. 9 represent coherence squared between OLR and 850-hPa wind, and vectors represent the phase by which wind anomalies lag OLR anomalies, increasing in the clockwise direction. A phase

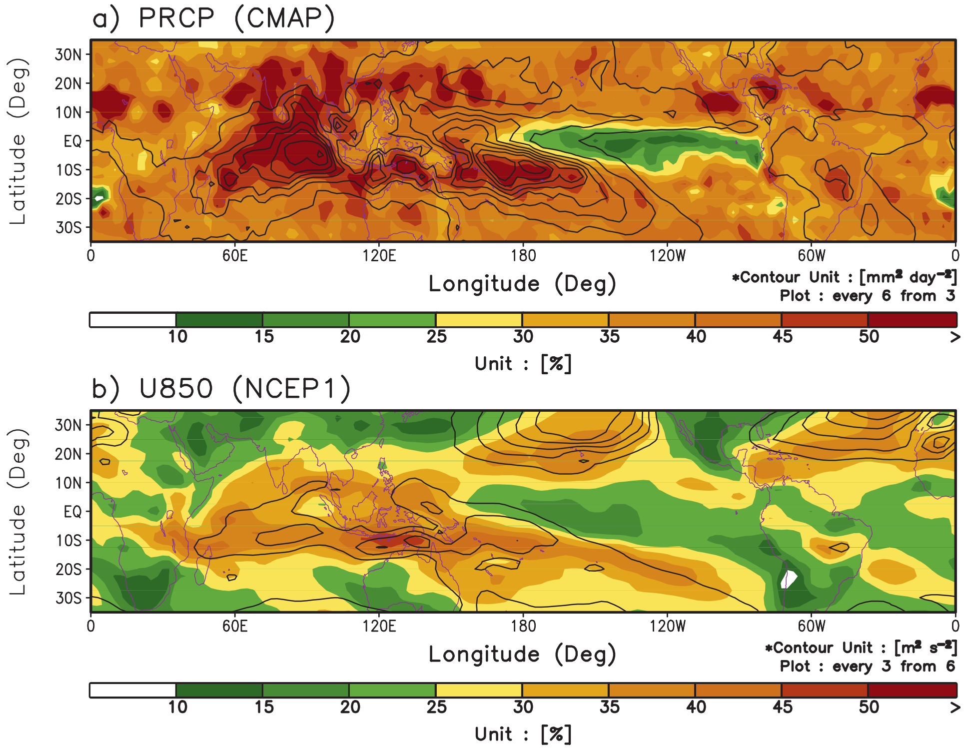

FIG. 4. As in Fig. 3, except for November–April.

of 0° is represented by a vector directed upward. Compared with Fig. 8, the axes of frequency and wavenumber have been switched, but eastward and westward propagation are still represented in the right and left sides of the diagrams, respectively.

Figure 9 indicates a high coherence squared (peaking at greater than 0.45) between convection and 850-hPa zonal winds at wavenumbers and frequencies characteristic of the MJO, with westerly (easterly) anomalies lagging suppressed (enhanced) convection by about 235 degrees

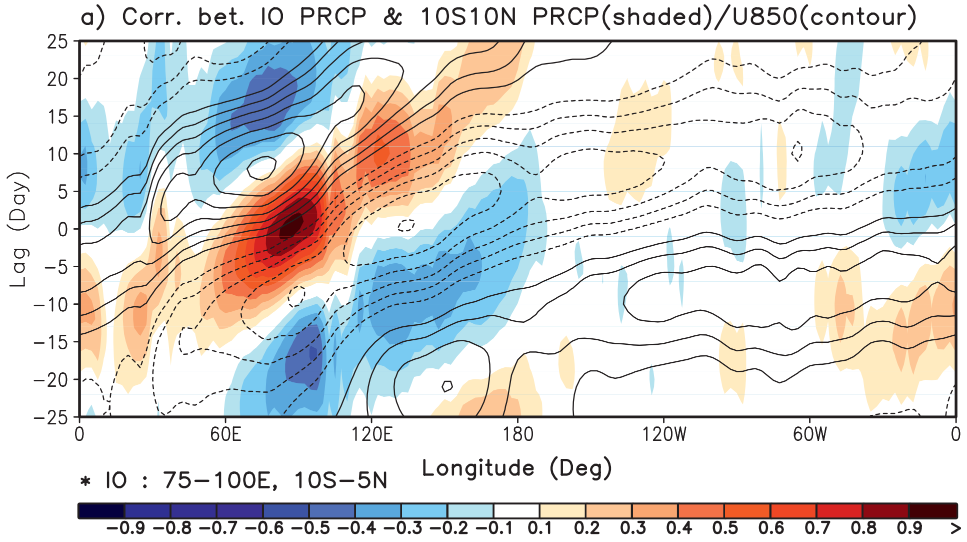

FIG. 5. November–April lag–longitude diagram of 10°N–10°S-averaged intraseasonal precipitation anomalies (colors) and intraseasonal 850-hPa zonal wind anomalies (contours) correlated against intraseasonal precipitation at the Indian Ocean reference point (Indian region in Table 2). Contours and colors are plotted every 0.1. The zero line is not shown.

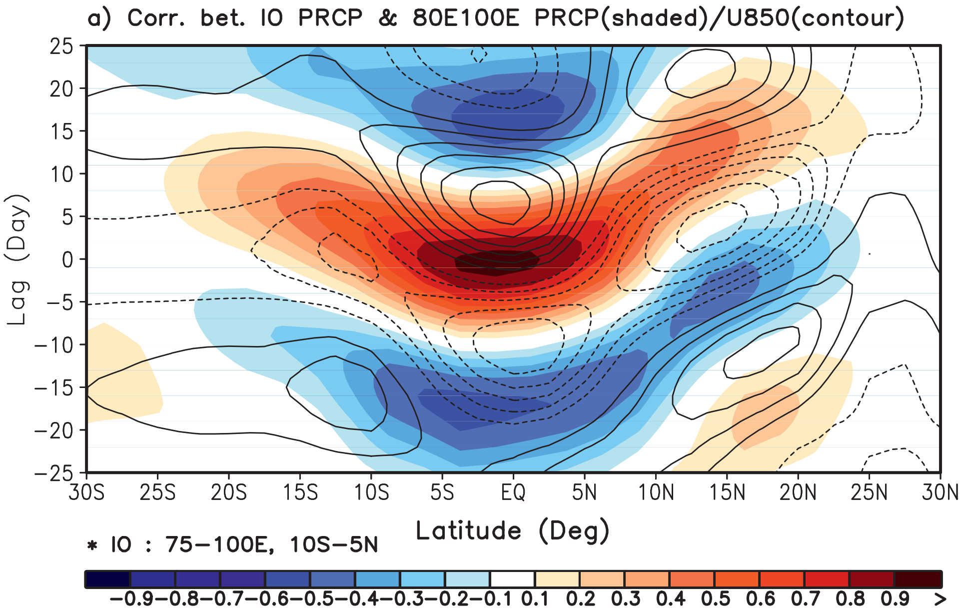

FIG. 6. May–October lag–latitude diagram of 80°–100°E-averaged intraseasonal precipitation anomalies (colors) and intraseasonal 850-hPa zonal wind anomalies (contours) correlated against intraseasonal precipitation at the Indian Ocean reference point at the equator. Contours and colors are plotted every 0.1. The zero line is not shown.

of phase. Another interpretation of Fig. 9 is that westerly (easterly) MJO wind anomalies lag enhanced (suppressed) convection by about an eighth of a cycle, or roughly 5 days at 40-day period. As has been described in the literature (e.g., Zhang et al. 2006), climate models have trouble simulating this high degree of coherence and ~5-day phase lag between convection and winds that is observed. Another notable feature of the cross spectra is that they directly capture and quantify convectively coupled equatorial Kelvin (peak coherence squared exceeding 0.3 for eastward wavenumbers 2–5 with periods of 5–10 days) and $n = 1$ Rossby (peak coherence exceeding 0.2 for westward wavenumbers 2–4 with periods of 25–50 days) wave modes in the symmetric spectrum, and mixed Rossby–gravity wave modes in the antisymmetric spectrum without the need to compute a background spectrum (Hendon and Wheeler 2008).

An efficient way to extract the salient features of the MJO is by multivariate EOF analysis using equatorial-averaged (15°N–15°S) anomalies of 850-hPa zonal winds, 200-hPa zonal winds, and OLR (Wheeler and Hendon 2004). The wind and OLR fields were individually normalized by the square root of the zonal mean of their temporal variance before input into the covariance matrix used to conduct the EOF analysis. This diagnostic provides a test of whether the correct phase relationship between equatorial convection and wind anomalies is produced: a relationship that is sometimes misrepresented in models (e.g., Maloney and Hartmann 2001). Figure 10 shows combined EOF1 and EOF2 derived for intraseasonal filtered NOAA OLR, and NCEP1 850- and 200-hPa zonal winds using all seasons of data during 1979–2005. Here we note the key features of the MJO, including the out-of-phase relationship between lower- and upper-tropospheric wind anomalies, the predominance of lower-tropospheric westerly anomalies near and to the west of enhanced convection, the concentrated amplitude of convection anomalies in the Eastern Hemisphere, and the strong amplitude of wind anomalies across both the Eastern and Western Hemispheres, particularly at upper levels. Importantly, as described in Wheeler and Hendon (2004), these equatorial EOF structures are virtually independent of season. Thus, these all-season EOFs can be used to develop MJO composites during both boreal summer and winter.

The overall variance accounted for by each EOF is indicated in Fig. 10. Calculation of the variance of individual fields (i.e., OLR, U850, U200) accounted for by each EOF is also recommended, as indicated in the figure. Many climate simulations produce leading EOFs for convective fields that explain relatively small amounts of the variance compared to observations (e.g., Waliser et al. 2003a; Zhang et al. 2006), and so this latter diagnostic provides a quantifiable measure of a model's ability to faithfully simulate the strength of the MJO. In observations the leading pair of EOFs account for 13%–16% of the variance of the intraseasonally filtered OLR data.

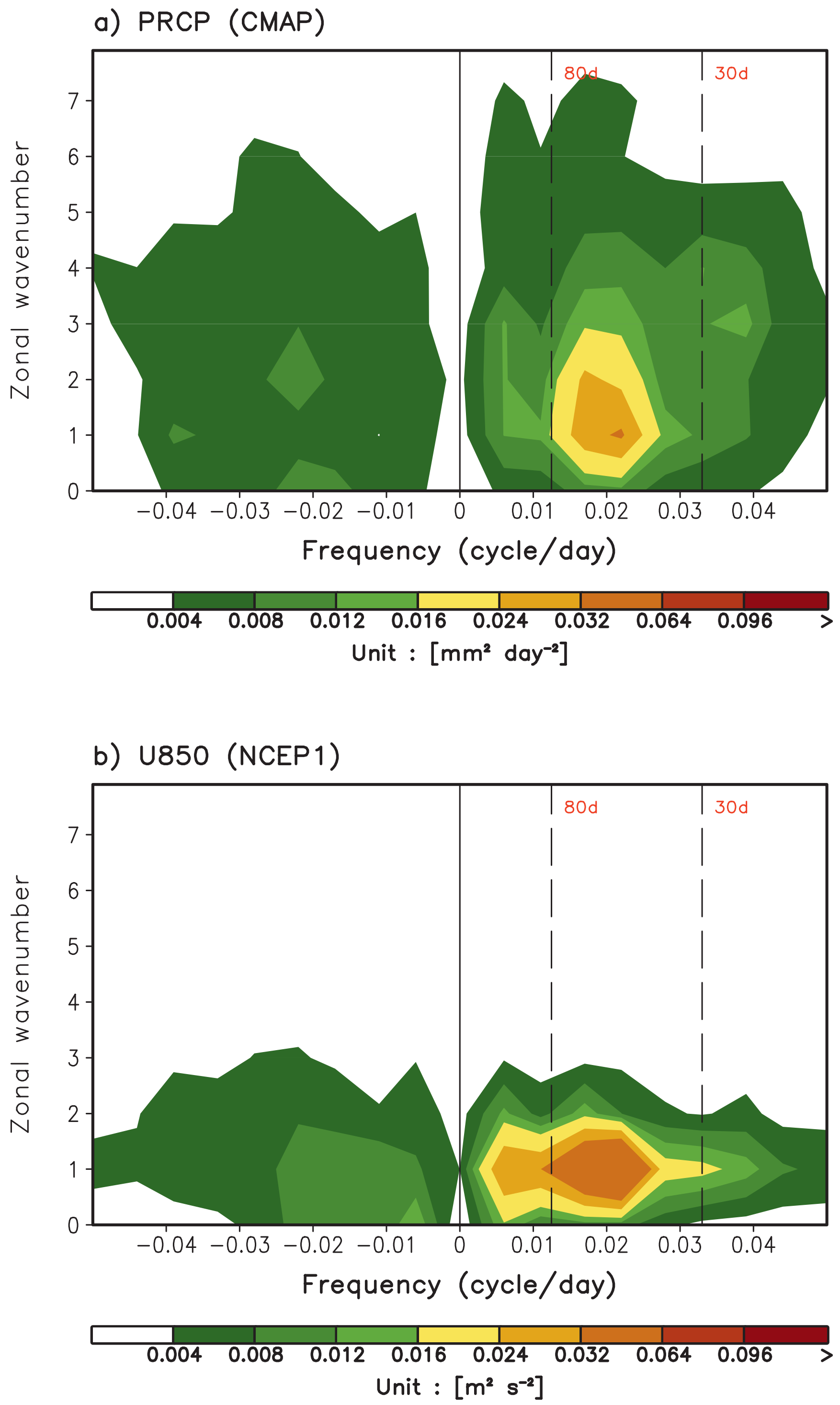

FIG. 7. May–October wavenumber-frequency spectra of 10°N–10°S-averaged (a) CMAP precipitation and (b) NCEP1 850-hPa zonal wind. Individual May–October spectra were calculated for each year, and then averaged over all years of data. Only the climatological seasonal cycle and time mean for each May–October segment were removed before calculation of the spectra. Units for the precipitation (zonal wind) spectrum are mm^2 day^{-2} (m^2 s^{-2}) per frequency interval per wavenumber interval. The bandwidth is (180 $day)^{-1}$.

Fig. 7 live 4/C

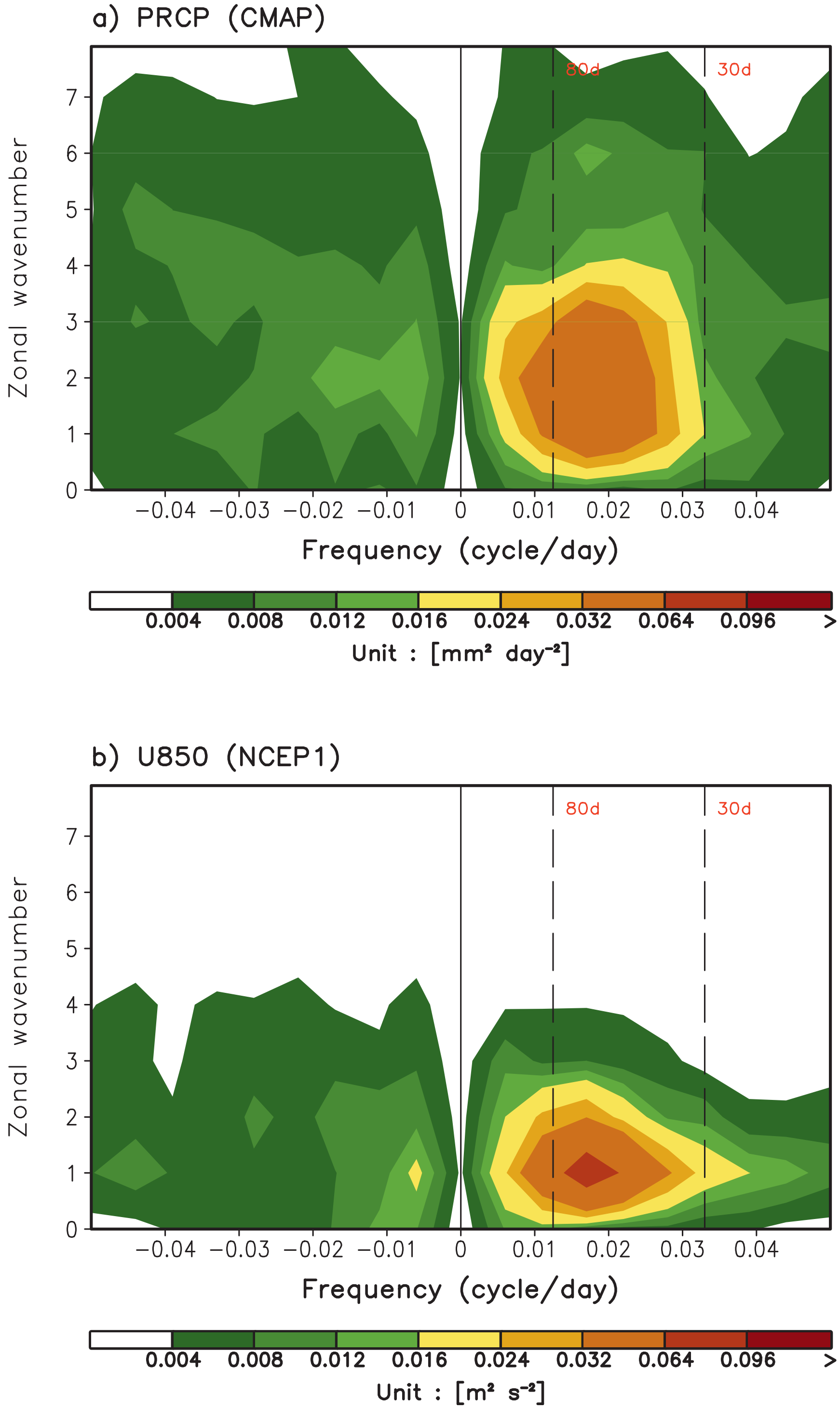

FIG. 8. As in Fig. 7, except for November–April.

Figure 10c shows the lag correlation between the PCs of the first two multivariate EOFs. The PCs are correlated at greater (less) than 0.7 (−0.7) when PC1 leads (lags) PC2 by about 10 days (−10 days). This phase relationship indicates that the leading multivariate EOFs are a quadrature pair, representing coherent eastward-propagating intraseasonal variability in precipitation and winds along the equator with period near 40 days, a fundamental criterion that a simulated MJO must meet. However, such behavior

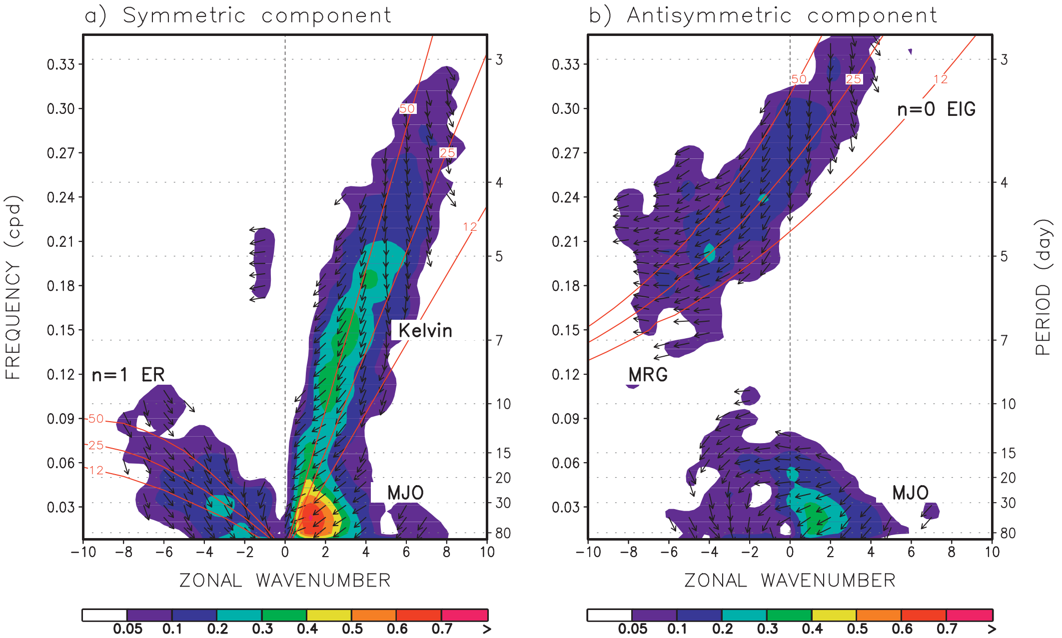

FIG. 9. Coherence squared (colors) and phase lag (vectors) between NOAA AVHRR OLR and NCEP1 850-hPa zonal wind. Here is shown (a) the symmetric spectrum, and (b) the antisymmetric spectrum. Spectra were computed for individual latitudes, and then averaged over 0°–10°. Computations are conducted using data in all seasons on 256-day segments, overlapping by 206 days. Vectors represent the phase by which wind anomalies lag OLR anomalies, increasing in the clockwise direction. A phase of 0° is represented by a vector directed upward. Dispersion curves for the ($n = -1$) Kelvin, $n = 1$ equatorial Rossby (ER), $n = 0$ eastward intertio-gravity (EIG), and mixed Rossby–gravity (MRG) modes corresponding to three equivalent depths (h = 12, 25, and 50 m) in the shallow water equations are overlaid (red contours). MJO is defined as the spectral components within zonal wavenumbers 1 to 3 and having periods 30 to 80 days.

is not always exhibited by models (e.g., Lin et al. 2006).

Another crucial test of a climate model is whether its leading multivariate EOFs derived from bandpass-filtered data represent a physically meaningful mode of variability. For example, red noise or white noise that is bandpass filtered to intraseasonal periods might produce plausible looking large-scale structures in the leading EOFs that could be misinterpreted to represent a physically distinct intraseasonal oscillation. Thus, a diagnostic to avoid such pitfalls is to project the leading EOFs derived from filtered data onto unfiltered data (with only the seasonal cycle removed), and then compute the frequency spectrum of the resulting unfiltered PCs (e.g., see Maloney and Hartmann 1998). If the power spectrum exhibits a significant spectral peak at intraseasonal periods, confidence is increased that the leading EOF(s) represent a meaningful intraseasonal mode of variability. Such an analysis is displayed in Fig. 10d for multivariate EOF 1. It is noted that the observed power spectrum clearly shows a prominent 30–80-day peak.

Level 2 diagnostics include a test of a model's ability to simulate the (horizontal and vertical) spatial–temporal structure of intraseasonal variability. The two leading multivariate EOFs shown in Fig. 10 are used to derive a composite MJO life cycle for boreal winter or boreal summer, as described in Wheeler and Hendon (2004). The MJO is defined to be strong during periods when PC1^2 + PC2^2 exceeds 1 (where PC1 and PC2 each have unit standard deviation), and these periods of high amplitude are retained in the composite analysis. The phase of the MJO can be related to the inverse tangent of the ratio of PC2 to PC1. For each phase, composites are generated by averaging across all days that exceed the specified amplitude threshold. The number of days meeting the amplitude criterion for each phase will be displayed to the right of each panel in the composite plots.

A composite MJO life cycle featuring intraseasonal precipitation and surface wind anomalies for boreal summer is displayed in Fig. 11, and a corresponding boreal winter composite is displayed in Figs. 12. Each panel in the composite life cycle is approximately 6 days apart. Features of these composites that serve as benchmark comparisons to simulations include 1) the pronounced seasonality in off-equatorial winds and precipitation (e.g., defined northward propagation in

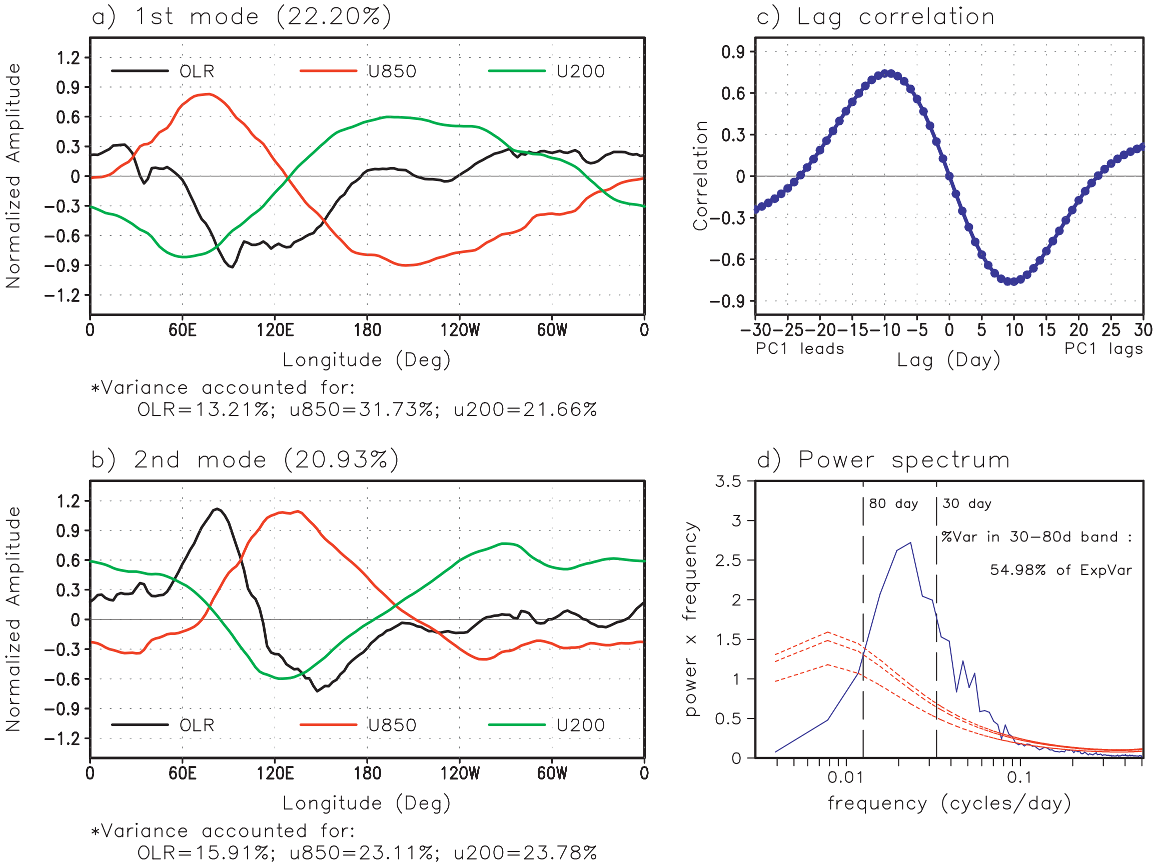

FIG. 10. All-season multivariate (a) first and (b) second combined EOF (CEOF) modes of 20–100-day 15°S–15°N-averaged NCEP1 850-hPa and 200-hPa zonal wind and AVHRR OLR. The total variance accounted for by each mode is shown (in parentheses at top), as is the variance of each individual field that is accounted for (at bottom). (c) The lag correlation of the leading PC is shown. (d) The time series spectrum of the unfiltered PC derived by projecting CEOF1 onto the unfiltered data matrix is shown. Red lines in (d) show the red noise spectrum and upper 90% and 95% confidence limits on this red noise spectrum.

the Eastern Hemisphere and strong east Pacific warm pool variability during boreal summer), consistent with the variance and % variance given in Figs. 3 and 4. Many models exhibit weak seasonality in the nature of their intraseasonal variability (e.g,. Slingo et al. 1996; Zhang et al. 2006). 2) The phase relationship between the spatial structures of precipitation and wind, including surface winds. When also considering the mean state, such a phase relationship is important to the MJO surface energy budget, with implications for air–sea interactions and wind-induced flux forcing of convection (e.g., Hendon 2000; Inness et al. 2003; Bellon et al. 2008). 3) The longitudinal extent of propagation in convection anomalies. Many climate models split intraseasonal convective anomalies into two centers straddling the equator (e.g., Waliser et al. 2003a; Maloney and Sobel 2004; Zhang et al. 2006). It is noted however that the equatorial-averaged behavior in the composite life cycles of Figs. 11 and 12 is approximately independent of season, consistent with our ability to use an all-season multivariate EOF index to define MJO behavior during both boreal winter and summer.

Another example of composite life cycle evolution detailed in the diagnostics package is the coevolution of SST and precipitation for boreal summer and boreal winter (Figs. 13 and 14). A motivation for such an analysis is to illustrate the phase relationship of anomalous SST relative to anomalous convection, particularly the anomalously warm SST that develops before the onset of MJO convection. The amplitude of SST anomalies, and the different SST evolution in boreal summer versus boreal winter (e.g., northward propagation of SST anomalies in the Eastern Hemisphere during boreal summer), may be compared to coupled models to infer whether air–sea coupling may regulate the amplitude of simulated intraseasonal variability. While many studies suggest that ocean coupling may

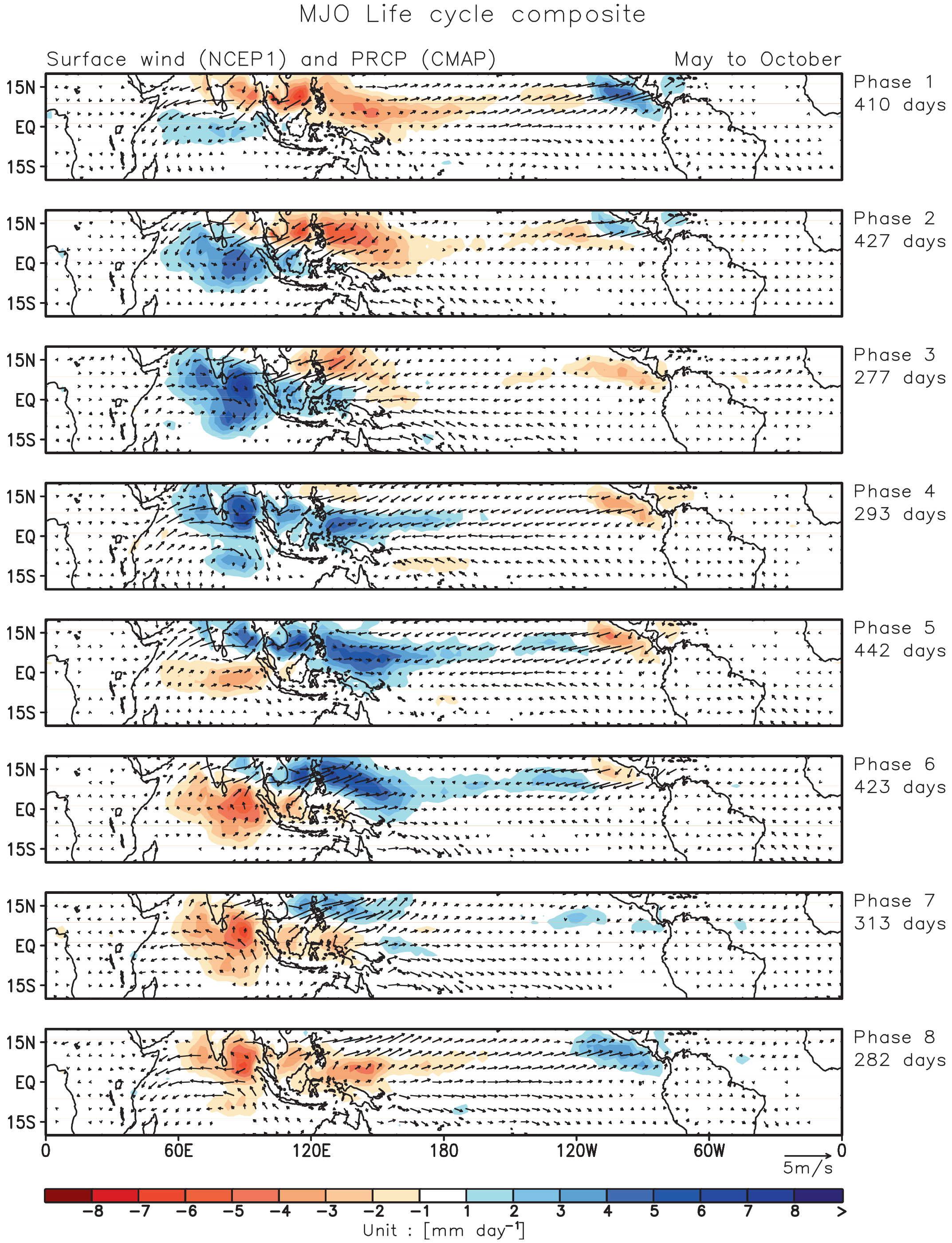

FIG. 11. Composite May–October 20–100-day CMAP precipitation (color) and NCEP1 surface wind anomalies (vectors) as a function of MJO phase. Zonal wind anomalies statistically significant at 99% based on Student's *t* test are drawn. The reference vector in units of m s^{-1} is shown at the bottom right. The number of days used to generate the composite for each phase is shown to the right of each panel.

help increase the amplitude of intraseasonal variability in climate models (e.g., Waliser et al. 1999b; Fu and Wang 2004; Sperber et al. 2005), other simulations suggest that if a model cannot reproduce the correct phase relationships among surface fluxes, convection, and SST anomalies, ocean coupling may have a deleterious effect on simulated intraseasonal variability (e.g., Hendon 2000).

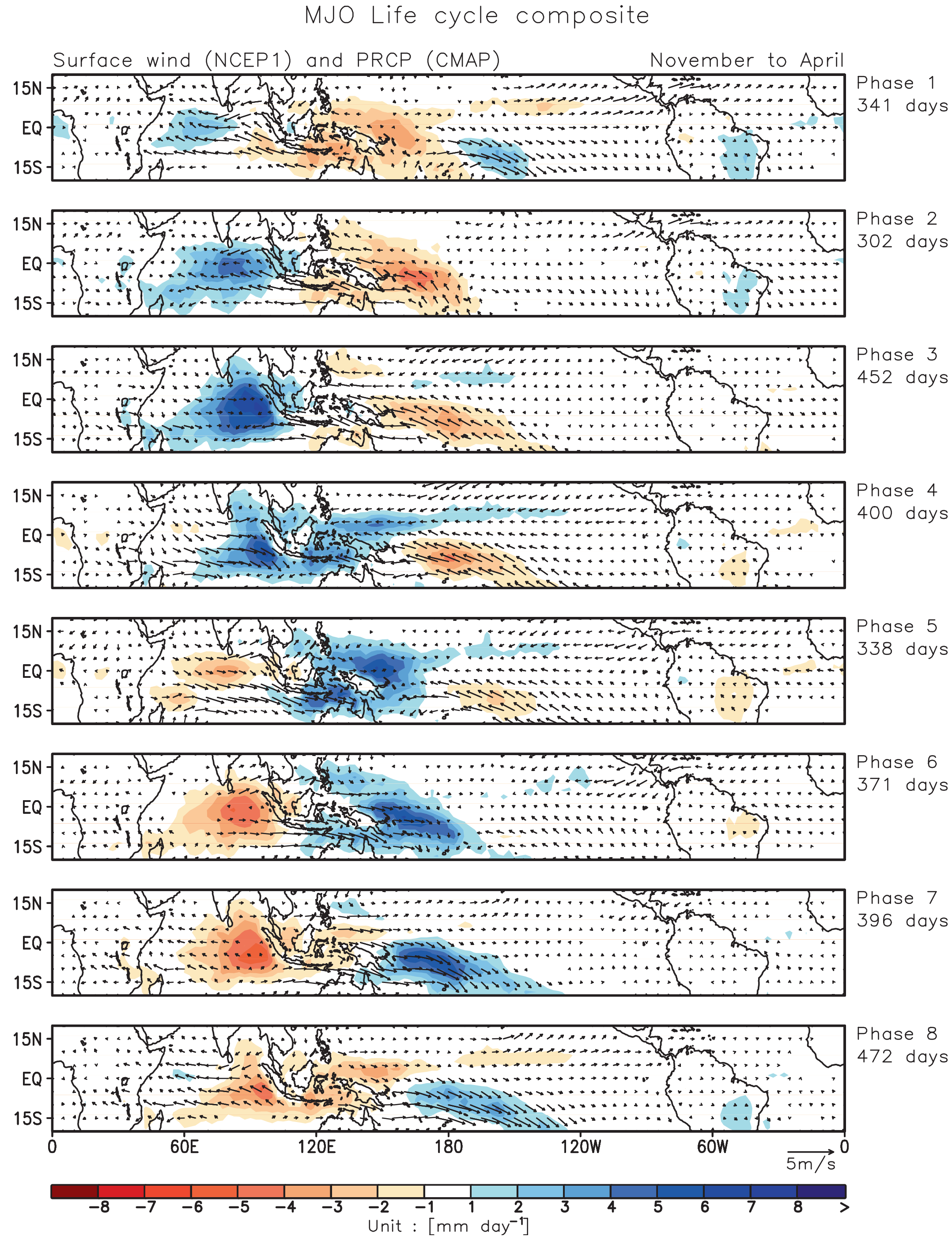

FIG. 12. Same as Fig. 11, except for November–April.

4. Summary

Accurate forecasts and simulations of the MJO are of great interest to weather and climate prediction. Yet most current global models fail to reproduce even the gross features of the MJO in spite of tremendous efforts made to improve model physics and the use of higher model resolution. The lack of standard diagnostics of the MJO has made difficult the comparison of model simulations of the MJO, the exploration of common deficiencies that contribute to their failure, and the evaluation and tracking of the improvement in MJO

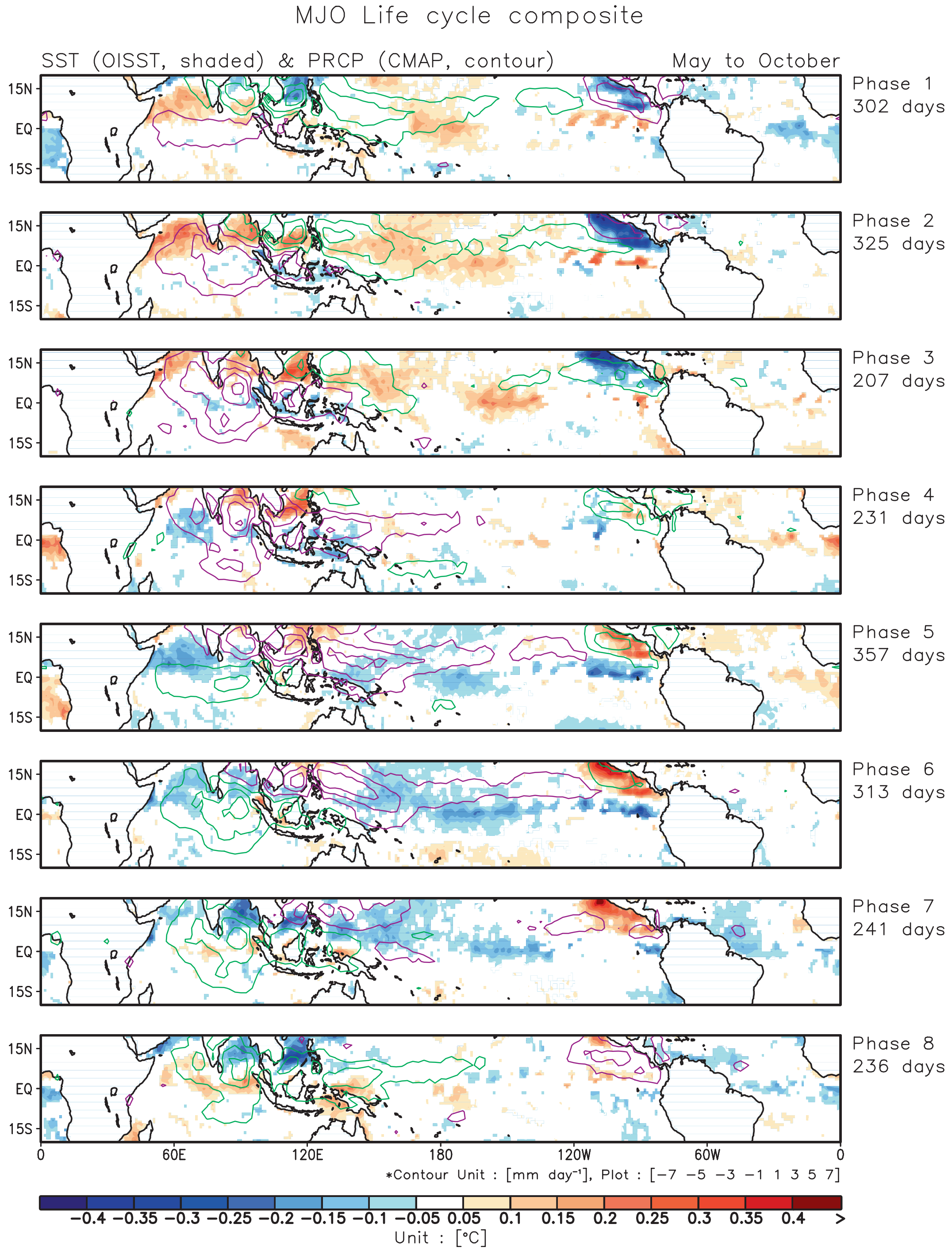

FIG. 13. Composite May–October 20–100 day OISST (color, units: °C; 4 Jan 1985–31 Dec 2005) and CMAP precipitation anomalies (contours) as a function of MJO phase. SST anomalies statistically significant at 99% based on Student's *t* test are drawn. Precipitation anomalies are plotted every 2 mm day^{-1}, starting at 1 mm day^{-1}. The number of days used to generate the composite for each phase is shown to the right of each panel.

Fig. 13 live 4/C

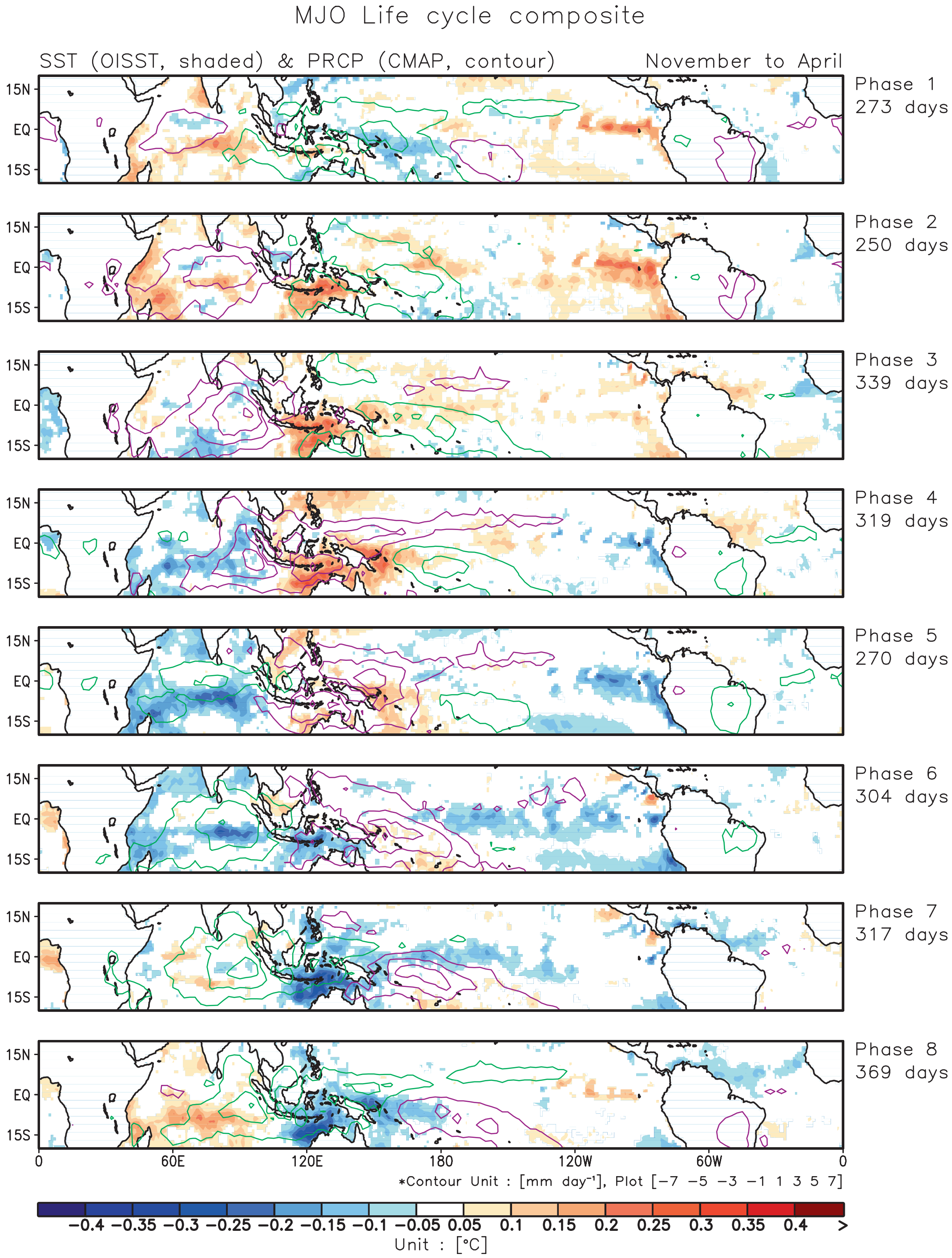

FIG. 14. Same as Fig. 13, except for November–April.

simulations. The purpose of this article is to recommend a set of such diagnostics using the following strategies:

(i) The diagnostics have been chosen to concentrate on and quantify what we feel are the most important and essential features of the MJO and its dynamics, yet simple enough for relatively easy understanding and calculation.

(ii) The MJO is defined such that it consists of both eastward propagation across the Indian and Pacific Oceans in summer and winter, and northward propagation during boreal summer. Because of its distinct northward propagation, the MJO diagnostics are calculated separately for boreal summer and winter, where appropriate.

(iii) All observation-based data (e.g., precipitation, OLR, and zonal winds) are based on either satellite remote sensing or global reanalyses. To account for measurement, retrieval and assimilation uncertainties, more than one data source are selected for each variable where possible (section 2). Current discrepancies between different model simulations of the MJO and any of these observation-based data are much greater than between any two observation-based datasets.

(iv) Supplemental diagnostics are recommended to include mean states of certain variables (SST, zonal winds, precipitation) and interannual variability of the MJO (Table 4). They may help understand the causes of erroneous behaviors of a simulated MJO and/or illustrate shortcomings in the multiscale interactions of a model (section 3a).

(v) The main part of the recommended diagnostics includes two levels.

The level 1 diagnostics (section 3c; Table 1) provide an initial assessment of intraseasonal variability in general and the most basic features of the MJO that can be easily calculated using standard tools without expertise in the MJO. The maps of intraseasonal variance (Figs. 3 and 4) and time spectra for key regions (Table 2) help reveal whether a model produces robust intraseasonal variability and its correct seasonality. The lag–longitude and lag–latitude correlations (Figs. 5 and 6) examine whether the simulated intraseasonal variability possesses eastward and northward propagations at the observed phase speeds, which are the most basic features of the MJO. The single variable EOF analysis tests whether MJO signals in a given field can be objectively isolated from the remainder of the intraseasonal variability.

If the level 1 diagnostics indicate that the model is indeed able to reproduce the basic features of the MJO, the level 2 diagnostics (section 3d; Table 3) would further detail the quantitative properties of the MJO using more sophisticated tools. The wavenumber-frequency spectra (Figs. 7 and 8) identify the intraseasonal spectral peak and quantify its eastward–westward power ratio, a measure of the robustness in the eastward propagation of the MJO. The coherence and phase relation between the zonal wind and convection components of the MJO are quantified by the cross-spectrum analysis (Fig. 9), which also demonstrates the distinctions between the MJO and other equatorial waves. The key test for assessing a model's ability to reproduce the MJO, including its time scale, phase speed, coherent spatial–temporal structures in zonal wind and convection, is to see whether its MJO signals can be extracted using a multivariate EOF analysis (Fig. 10). This multivariate EOF analysis also sets the stage for composite analyses of the MJO to examine mechanistic, structural, and evolutionary details during different phases of its life cycle (Figs. 11 and 12). For coupled models, similar composites can be made to include SST (Figs. 13 and 14).

The diagnostics recommended here are based on the availability of reliable observation-based data (e.g., satellite and reanalyses products) and confidence in our knowledge of the MJO. MJO diagnostics for other variables (e.g., cloud and boundary layer structure, latent and radiative heating) will be recommended in the future when reliable observations are available for a sufficiently long period. In addition, a number of recommendations related to MJO diagnostics/metrics were made based on the discussions at a recent CLIVAR-sponsored MJO workshop organized by the MJOWG (Sperber and Waliser 2008). These include: 1) converting the diagnostics developed here, or new ones, into scalar metrics/values to more easily quantify multimodel comparison results and for quantitatively tracking model fidelity, 2) develop process-oriented diagnostics that improve our insight into the physical mechanisms necessary for robust simulation of the MJO, and 3) continue to explore the multiscale interactions and vertical structure of the MJO. Other avenues for diagnostic development are more precise characterization of the boreal summer northward propagating events (e.g., Fu et al. 2003; Krishnamurthy and Shukla 2008; Sperber and Annamalai 2008) and the discrimination between initial MJO events (i.e., with no precursor) and those that occur in succession (Matthews 2008). At present, the MJOWG is working on applying the MJO diagnostics to a set of recent GCM simulations and on defining and implementing a metric for MJO predictions; the results of these activities will be reported on in forthcoming papers.

In conclusion, we recommend the level 1 diagnostics be applied to all model evaluation exercises and the level 2 diagnostics only to models with capability of producing the basic features of the MJO as demonstrated by the level-1 diagnostics. It is our hope that when all model evaluations adopt the set of diagnostics recommended here, we will be in a much better position to compare models, identify common model deficiencies, and track model improvement in regard to MJO simulations.

Acknowledgments. The MJOWG wishes to acknowledge and thank U.S. CLIVAR and International CLIVAR for supporting this working group and its activities. We would like to specifically acknowledge the administrative support on behalf of the MJOWG by

Cathy Stevens of the U.S. CLIVAR Office. KRS was supported under the auspices of the U.S. Department of Energy Office of Science, Climate Change Prediction Program by Lawrence Livermore National Laboratory under Contract DE-AC52-07NA27344. DEW's contributions to this study were carried out on behalf of the Jet Propulsion Laboratory, California Institute of Technology, under a contract with the National Aeronautics and Space Administration (NASA). EDM was supported by the NSF Climate and Large-Scale Dynamics Program under Grant ATM-063234, and by NOAA CPPA Award NA05OAR4310006. CZ was support by NSF Grant ATM0739402 and by the NOAA Office of Global Programs through the Cooperative Institute for Marine and Atmospheric Studies (CIMAS). D. Kim and I. Kang were supported by the Korea Meteorological Administration Research and Development Program under Grant CATER_2006-4206 and BK21 program.

REFERENCES

Annamalai, H., and K. R. Sperber, 2005: Regional heat sources and the active and break phases of boreal summer intraseasonal (30–50 day) variability. *J. Atmos. Sci.,* **62,** 2726–2748.

Arkin, P. A., and B. N. Meisner, 1987: The relationship between large-scale convective rainfall and cold cloud over the western hemisphere during 1982–1984. *Mon. Wea. Rev.,* **115,** 51–74.

Barlow, M., and D. Salstein, 2006: Summertime influence of the Madden–Julian oscillation on daily rainfall over Mexico and Central America. *Geophys. Res. Lett.,* **33,** L21708, doi:10.1029/2006GL027738.

Bellon, B., A. Sobel, and J. P. Vialard, 2008: Ocean–atmosphere coupling in the monsoon intraseasonal oscillation: A simple model study. *J. Climate,* **21,** 5254–5270.

Bergman, J. W., H. H. Hendon, and K. M. Weickmann, 2001: Intraseasonal air–sea interactions at the onset of El Niño. *J. Climate,* **14,** 1702–1719.

Bernie, D. J., S. J. Woolnough, J. M. Slingo, and E. Guilyardi, 2005: Modeling diurnal and intraseasonal variability of the ocean mixed layer. *J. Climate,* **18,** 1190–1202.

Bessafi, M., and M. C. Wheeler, 2006: Modulation of South Indian Ocean tropical cyclones by the Madden–Julian oscillation and convectively coupled equatorial waves. *Mon. Wea. Rev.,* **134,** 638–656.

Chen, S. S., R. A. Houze, and B. E. Mapes, 1996: Multiscale variability of deep convection in relation to large-scale circulation in TOGA COARE. *J. Atmos. Sci.,* **53,** 1380–1409.

Duchon, C. E., 1979: Lanczos filtering in one and two dimensions. *J. Appl. Meteor.,* **18,** 1016–1022.

Duffy, P. B., B. Govindasamy, J. P. Iorio, J. Milovich, K. R. Sperber, K. E. Taylor, M. F. Wehner, and S. L. Thompson, 2003: High-resolution simulations of global climate, Part 1: Present climate. *Climate Dyn.,* **21,** 371–390.

ECMWF, 2004: *Proceedings of the ECMWF/CLIVAR Workshop on Simulation and Prediction of Intra-Seasonal Variability with Emphasis on the MJO*. Reading, United Kingdom, ECMWF, 269 pp.

Ferranti, L., T. N. Palmer, F. Molteni, and K. Klinker, 1990: Tropical–extratropical interaction associated with the 30–60-day oscillation and its impact on medium and extended range prediction. *J. Atmos. Sci.,* **47,** 2177–2199.

Frank, W. M., and P. E. Roundy, 2006: The role of tropical waves in tropical cyclogenesis. *Mon. Wea. Rev.,* **134,** 2397–2417.

Fu, X., and B. Wang, 2004: Differences of boreal-summer intraseasonal oscillations simulated in an atmosphere–ocean coupled model and an atmosphere-only model. *J. Climate,* **17,** 1263–1271.

Fu, X. H., B. Wang, T. Li, and J. P. McCreary, 2003: Coupling between northward-propagating, intraseasonal oscillations and sea surface temperature in the Indian Ocean. *J. Atmos. Sci.,* **60,** 1733–1753.

Goswami, B. N., 2005: South Asian summer monsoon. *Intraseasonal Variability of the Atmosphere–Ocean Climate System*, W. K. M. Lau and D. E. Waliser, Eds., Springer, 19–62.

Gualdi, S., A. Navarra, and M. Fischer, 1999a: The tropical intraseasonal oscillation in a coupled ocean–atmosphere general circulation model. *Geophys. Res. Lett.,* **26,** 2973–2976.

——, ——, and G. Tinarelli, 1999b: The interannual variability of the Madden–Julian oscillation in an ensemble of GCM simulations. *Climate Dyn.,* **15,** 643–658.

Gupta, S. K., D. P. Kratz, P. W. Stackhouse Jr., and A. C. Wilber, 2001: The Langley Parameterized Shortwave Algorithm (LPSA) for surface radiation budget studies (Version 1.0). NASA/TP-2001-211272, 31 pp.

Hendon, H. H., 2000: Impact of air–sea coupling on the Madden–Julian oscillation in a general circulation model. *J. Atmos. Sci.,* **57,** 3939–3952.

——, and B. Liebmann, 1990: The intraseasonal (30–50 day) oscillation of the Australian summer monsoon. *J. Atmos. Sci.,* **47,** 2909–2923.

——, and M. L. Salby, 1994: The life-cycle of the Madden–Julian oscillation. *J. Atmos. Sci.,* **51,** 2225–2237.

——, and M. C. Wheeler, 2008: Some space–time spectral analyses of tropical convection and planetary-scale waves. *J. Atmos. Sci.,* **65,** 2936–2948.

——, C. D. Zhang, and J. D. Glick, 1999: Interannual variation of the Madden–Julian oscillation during austral summer. *J. Climate,* **12,** 2538–2550.

——, B. Liebmann, M. Newman, J. D. Glick, and J. E. Schemm, 2000: Medium-range forecast errors associated with active episodes of the Madden–Julian oscillation. *Mon. Wea. Rev.,* **128,** 69–86.

——, M. C. Wheeler, and C. D. Zhang, 2007: Seasonal dependence of the MJO–ENSO relationship. *J. Climate,* **20,** 531–543.

Higgins, R. W., and K. C. Mo, 1997: Persistent North Pacific circulation anomalies and the tropical intraseasonal oscillation. *J. Climate,* **10,** 223–244.

——, J. K. E. Schemm, W. Shi, and A. Leetmaa, 2000: Extreme precipitation events in the western United States related to tropical forcing. *J. Climate,* **13,** 793–820.

Huffman, G. J., R. F. Adler, M. M. Morrissey, D. T. Bolvin, S. Curtis, R. Joyce, B. McGavock, and J. Susskind, 2001: Global precipitation at one-degree daily resolution from multisatellite observations. *J. Hydrometeor.,* **2,** 36–50.

ICTP, 2006: *Proceedings of the Workshop on the Organization and Maintenance of Tropical Convection and the Madden–Julian Oscillation*. Trieste, Italy, International Centre for Theoretical Physics, 13 pp.

Inness, P. M., and J. M. Slingo, 2003: Simulation of the Madden–Julian oscillation in a coupled general circulation model.

Part I: Comparison with observations and an atmosphere-only GCM. *J. Climate,* **16,** 345–364.

——, ——, E. Guilyardi, and J. Cole, 2003: Simulation of the Madden–Julian oscillation in a coupled general circulation model. Part II: The role of the basic state. *J. Climate,* **16,** 365–382.

Jones, C., 2000: Occurrence of extreme precipitation events in California and relationships with the Madden–Julian oscillation. *J. Climate,* **13,** 3576–3587.

——, D. E. Waliser, K. M. Lau, and W. Stern, 2004a: Global occurrences of extreme precipitation and the Madden–Julian oscillation: Observations and predictability. *J. Climate,* **17,** 4575–4589.

——, ——, ——, and ——, 2004b: The Madden–Julian oscillation and its impact on Northern Hemisphere weather predictability. *Mon. Wea. Rev.,* **132,** 1462–1471.

Kalnay, E., and Coauthors, 1996: The NCEP/NCAR 40-Year Reanalysis Project. *Bull. Amer. Meteor. Soc.,* **77,** 437–471.

Kanamitsu, M., W. Ebisuzaki, J. Woollen, S.-K. Yang, J. J. Hnilo, M. Fiorino, and G. L. Potter, 2002: NCEP-DOE AMIP-II Reanalysis (R-2). *Bull. Amer. Meteor. Soc.,* **83,** 1631–1643.

Kemball-Cook, S., B. Wang, and X. Fu, 2002: Simulation of the ISO in the ECHAM4 model: The impact of coupling with an ocean model. *J. Atmos. Sci.,* **59,** 1433–1453.

Kessler, W. S., 2005: The oceans. *Intraseasonal Variability of the Atmosphere–Ocean Climate System,* W. K. M. Lau and D. E. Waliser, Eds., Springer, 175–222.

——, 2001: EOF representations of the Madden–Julian oscillation and its connection with ENSO. *J. Climate,* **14,** 3055–3061.

——, and R. Kleeman, 2000: Rectification of the Madden–Julian oscillation into the ENSO cycle. *J. Climate,* **13,** 3560–3575.

Kiladis, G. N., K. H. Straub, and P. T. Haertel, 2005: Zonal and vertical structure of the Madden–Julian oscillation. *J. Atmos. Sci.,* **62,** 2790–2809.

Krishnamurthy, V., and J. Shukla, 2008: Seasonal persistence and propagation of intraseasonal patterns over the Indian monsoon region. *Climate Dyn.,* **30,** 353–369, doi:10.1007/s00382-007-0300-7.

Kummerow, C., and Coauthors, 2000: The status of the Tropical Rainfall Measuring Mission (TRMM) after two years in orbit. *J. Appl. Meteor.,* **39,** 1965–1982.

Lau, K.-M., and P. H. Chan, 1988: Intraseasonal and interannual variations of tropical convection: A possible link between the 40–50 day oscillation and ENSO. *J. Atmos. Sci.,* **45,** 506–521.

——, and S. Shen, 1988: On the dynamics of intraseasonal oscillations and ENSO. *J. Atmos. Sci.,* **45,** 1781–1797.

Lau, W. K. M., 2005: El Niño Southern Oscillation connection. *Intraseasonal Variability of the Atmosphere–Ocean Climate System*, W. K. M. Lau and D. E. Waliser, Eds., Springer, 271–306.

Lau, W. K. M., and D. E. Waliser, 2005: *Intraseasonal Variability of the Atmosphere–Ocean Climate System*. Springer, 436 pp.

Lawrence, D. M., and P. J. Webster, 2002: The boreal summer intraseasonal oscillation: Relationship between northward and eastward movement of convection. *J. Atmos. Sci.,* **59,** 1593–1606.

Lee, M.-I., I.-S. Kang, J.-K. Kim, and B. E. Mapes, 2001: Influence of cloud-radiation interaction on simulating tropical intraseasonal oscillation with an atmospheric general circulation model. *J. Geophys. Res.,* **106** (D13), 14 219–14 233.

——, ——, and B. E. Mapes, 2003: Impacts of cumulus convection parameterization on aqua-planet AGCM simulations of tropical intraseasonal variability. *J. Meteor. Soc. Japan,* **81,** 963–992.

Liebmann, B., and D. L. Hartmann, 1984: An observational study of tropical midlatitude interaction on intraseasonal time scales during winter. *J. Atmos. Sci.,* **41,** 3333–3350.

——, and C. A. Smith, 1996: Description of a complete (interpolated) outgoing longwave radiation dataset. *Bull. Amer. Meteor. Soc.,* **77,** 1275–1277.

——, H. H. Hendon, and J. D. Glick, 1994: The relationship between tropical cyclones of the Western Pacific and Indian Oceans and the Madden–Julian oscillation. *J. Meteor. Soc. Japan,* **72,** 401–412.

Lin, J.-L., 2007: The double-ITCZ problem in IPCC AR4 coupled GCMs: Ocean–atmosphere feedback analysis. *J. Climate,* **20,** 4497–4525.

——, and Coauthors, 2006: Tropical intraseasonal variability in 14 IPCC AR4 climate models. Part I: Convective signals. *J. Climate,* **19,** 2665–2690.

Lorenz, D. J., and D. L. Hartmann, 2006: The effect of the MJO on the North American monsoon. *J. Climate,* **19,** 333–343.

Madden, R. A., and P. R. Julian, 1971: Detection of a 40–50 day oscillation in the zonal wind in the tropical Pacific. *J. Atmos. Sci.,* **28,** 702–708.

——, and ——, 1994: Observations of the 40–50-Day tropical oscillation—A review. *Mon. Wea. Rev.,* **122,** 814–837.

——, and ——, 2005: Historical perspective. *Intraseasonal Variability of the Atmosphere–Ocean Climate System,* W. K. M. Lau and D. E. Waliser, Eds., Springer, 1–18.

Maloney, E. D., 2002: An intraseasonal oscillation composite life cycle in the NCAR CCM3.6 with modified convection. *J. Climate,* **15,** 964–982.

——, and D. L. Hartmann, 1998: Frictional moisture convergence in a composite life cycle of the Madden–Julian oscillation. *J. Climate,* **11,** 2387–2403.

——, and ——, 2000a: Modulation of eastern North Pacific hurricanes by the Madden–Julian oscillation. *J. Climate,* **13,** 1451–1460.

——, and ——, 2000b: Modulation of hurricane activity in the Gulf of Mexico by the Madden–Julian oscillation. *Science,* **287,** 2002–2004.

——, and ——, 2001: The sensitivity of intraseasonal variability in the NCAR CCM3 to changes in convective parameterization. *J. Climate,* **14,** 2015–2034.

——, and S. K. Esbensen, 2003: The amplification of east Pacific Madden–Julian Oscillation convection and wind anomalies during June–November. *J. Climate,* **16,** 3482–3497.

——, and A. H. Sobel, 2004: Surface fluxes and ocean coupling in the tropical intraseasonal oscillation. *J. Climate,* **17,** 4368–4386.

——, and J. Shaman, 2008: Intraseasonal variability of the West African monsoon and Atlantic ITCZ. *J. Climate,* **21,** 2898–2918.

——, D. B. Chelton, and S. K. Esbensen, 2008: Subseasonal SST variability in the tropical eastern North Pacific during boreal summer. *J. Climate,* **21,** 4149–4167.

Matthews, A. J., 2000: Propagation mechanisms for the Madden–Julian Oscillation. *Quart. J. Roy. Meteor. Soc.,* **126,** 2637–2651.

——, 2004: Intraseasonal variability over tropical Africa during northern summer. *J. Climate,* **17,** 2427–2440.

——, 2008: Primary and successive events in the Madden–Julian oscillation. *Quart. J. Roy. Meteor. Soc.,* **134,** 439–453, doi:10.1002/qj.224.

Mechoso, C. R., and Coauthors, 1995: The seasonal cycle over the tropical Pacific in coupled ocean–atmosphere general-circulation models. *Mon. Wea. Rev.,* **123,** 2825–2838.

Mo, K. C., and R. W. Higgins, 1998: Tropical influences on California precipitation. *J. Climate,* **11,** 412–430.

Nakazawa, T., 1986: Intraseasonal variations of OLR in the tropics during the FGGE year. *J. Meteor. Soc. Japan,* **64,** 17–33.

Newman, M., P. D. Sardeshmukh, C. R. Winkler, and J. S. Whitaker, 2003: A study of subseasonal predictability. *Mon. Wea. Rev.,* **131,** 1715–1732.

Reynolds, R. W., T. M. Smith, C. Liu, D. B. Chelton, K. S. Casey, and M. G. Schlax, 2007: Daily high-resolution blended analyses for sea surface temperature. *J. Climate,* **20,** 5473–5496.

Rui, H., and B. Wang, 1990: Development characteristics and dynamic structure of tropical intraseasonal convection anomalies. *J. Atmos. Sci.,* **47,** 357–379.

Salby, M. L., and H. H. Hendon, 1994: Intraseasonal behavior of clouds, temperature, and motion in the tropics. *J. Atmos. Sci.,* **51,** 2207–2224.

Schubert, S., R. Dole, H. van den Dool, M. Suarez, and D. Waliser, 2002: Proceedings from a workshop on ''Prospects for improved forecasts of weather and short-term climate variability on subseasonal (2 week to 2 month) time scales.'' NASA/TM 2002-104606, Vol. 23, 171 pp.

Seo, K. H., J. K. E. Schemm, C. Jones, and S. Moorthi, 2005: Forecast skill of the tropical intraseasonal oscillation in the NCEP GFS dynamical extended range forecasts. *Climate Dyn.,* **25,** 265–284.

Shinoda, T., and H. H. Hendon, 1998: Mixed layer modeling of intraseasonal variability in the tropical Western Pacific and Indian Oceans. *J. Climate,* **11,** 2668–2685.

——, ——, and J. Glick, 1998: Intraseasonal variability of surface fluxes and sea surface temperature in the tropical western Pacific and Indian Oceans. *J. Climate,* **11,** 1685–1702.

Slingo, J. M., and Coauthors, 1996: Intraseasonal oscillations in 15 atmospheric general circulation models: Results from an AMIP diagnostic subproject. *Climate Dyn.,* **12,** 325–357.

——, P. Inness, and K. Sperber, 2005: Modeling. *Intraseasonal Variability of the Atmosphere–Ocean Climate System,* W. K. M. Lau and D. E. Waliser, Eds., Springer, 361–388.

Spencer, R. W., 1993: Global oceanic precipitation from the MSU during 1979–91 and comparisons to other climatologies. *J. Climate,* **6,** 1301–1326.

Sperber, K. R., 2003: Propagation and the vertical structure of the Madden–Julian Oscillation. *Mon. Wea. Rev.,* **131,** 3018–3037.

——, 2004: Madden–Julian variability in NCAR CAM2.0 and CCSM2.0. *Climate Dyn.,* **23,** 259–278.

——, and H. Annamalai, 2008: Coupled model simulations of boreal summer intraseasonal (30–50 day) variability, Part 1: Systematic errors and caution on use of metrics. *Climate Dyn.,* **31,** 345–372, doi:10.1007/s00382-008-0367-9.

——, and D. Waliser, 2008: New approaches to understanding, simulating, and forecasting the Madden–Julian oscillation. *Bull. Amer. Meteor. Soc.,* **89,** 1917–1920.

——, J. M. Slingo, and H. Annamalai, 2000: Predictability and the relationship between subseasonal and interannual variability during the Asian summer monsoon. *Quart. J. Roy. Meteor. Soc.,* **126,** 2545–2574.

——, and Coauthors, 2001: Dynamical seasonal predictability of the Asian summer monsoon. *Mon. Wea. Rev.,* **129,** 2226–2248.

——, S. Gualdi, S. Legutke, and V. Gayler, 2005: The Madden–Julian oscillation in ECHAM4 coupled and uncoupled general circulation models. *Climate Dyn.,* **25,** 117–140.

Straub, K. H., G. N. Kiladis, and P. E. Ciesielski, 2006: The role of equatorial waves in the onset of the South China Sea summer monsoon and the demise of El Niño during 1998. *Dyn. Atmos. Oceans,* **42,** 216–238.

Takayabu, Y. N., T. Iguchi, M. Kachi, A. Shibata, and H. Kanzawa, 1999: Abrupt termination of the 1997–98 El Nino in response to a Madden–Julian oscillation. *Nature,* **402,** 279–282.

Tian, B. J., D. E. Waliser, and E. J. Fetzer, 2006: Modulation of the diurnal cycle of tropical deep convective clouds by the MJO. *Geophys. Res. Lett.,* **33,** 20704, doi:10.1029/2006GL027752.

——, Y. L. Yung, D. E. Waliser, T. Tyranowski, L. Kuai, E. J. Fetzer, and F. W. Irion, 2007: Intraseasonal variations of the tropical total ozone and their connection to the Madden–Julian oscillation. *Geophys. Res. Lett.,* **34,** L08704, doi:10.1029/2007GL029451.

——, and Coauthors, 2008: Does the Madden–Julian oscillation influence aerosol variability? *J. Geophys. Res.,* **113,** D12215, doi:10.1029/2007JD009372.

Uppala, S. M., and Coauthors, 2005: The ERA-40 Re-Analysis. *Quart. J. Roy. Meteor. Soc.,* **131,** 2961–3012.

Vecchi, G. A., and N. A. Bond, 2004: The Madden–Julian Oscillation (MJO) and northern high latitude wintertime surface air temperatures. *Geophys. Res. Lett.,* **31,** L04104, doi:10.1029/2003GL018645.

Waliser, D. E., 2005: Predictability and forecasting. *Intraseasonal Variability of the Atmosphere–Ocean Climate System,* W. K. M. Lau and D. E. Waliser, Eds., Springer, 389–424.

——, 2006: Intraseasonal variability. *The Asian Monsoon*, B. Wang, Ed., Springer, 203–258.

——, C. Jones, J. K. E. Schemm, and N. E. Graham, 1999a: A statistical extended-range tropical forecast model based on the slow evolution of the Madden–Julian oscillation. *J. Climate,* **12,** 1918–1939.

——, K. M. Lau, and J.-H. Kim, 1999b: The influence of coupled sea surface temperatures on the Madden–Julian oscillation: A model perturbation experiment. *J. Atmos. Sci.,* **56,** 333–358.

——, Z. Zhang, K. M. Lau, and J.-H. Kim, 2001: Interannual sea surface temperature variability and the predictability of tropical intraseasonal variability. *J. Atmos. Sci.,* **58,** 2596–2615.

——, and Coauthors, 2003a: AGCM simulations of intraseasonal variability associated with the Asian summer monsoon. *Climate Dyn.,* **21,** 423–446.

——, R. Murtugudde, and L. Lucas, 2003b: Indo-Pacific ocean response to atmospheric intraseasonal variability. Part I: Austral summer and the Madden–Julian oscillation. *J. Geophys. Res.,* **108,** 3160, doi:10.1029/2002JC001620.

——, S. Schubert, A. Kumar, K. Weickmann, and R. Dole, 2003c: Proceedings from a workshop on ''Modeling, Simulation and Forecasting of Subseasonal Variability,'' NASA/TM 2003-104606, Vol. 25, 67 pp.

——, W. Stern, S. Schubert, and K. M. Lau, 2003d: Dynamic predictability of intraseasonal variability associated with the Asian summer monsoon. *Quart. J. Roy. Meteor. Soc.,* **129,** 2897–2925.

——, R. Murtugudde, P. Strutton, and J.-L. Li, 2005: Subseasonal organization of ocean chlorophyll: Prospects for prediction based on the Madden–Julian oscillation. *Geophys. Res. Lett.,* **32,** L23602, doi:10.1029/2005GL024300.

Wang, B., and H. Rui, 1990: Synoptic climatology of transient tropical intraseasonal convection anomalies: 1975–1985. *Meteor. Atmos. Phys.,* **44** (1-4), 43–61.

——, and X. Xie, 1997: A model for the boreal summer intraseasonal oscillation. *J. Atmos. Sci.,* **54,** 72–86.

Wang, W. Q., and M. E. Schlesinger, 1999: The dependence on convection parameterization of the tropical intraseasonal oscillation simulated by the UIUC 11-layer atmospheric GCM. *J. Climate,* **12,** 1423–1457.

Webster, P. J., and C. Hoyos, 2004: Forecasting monsoon rainfall and river discharge variability on 20–25-day time scales. *Bull. Amer. Meteor. Soc.,* **85,** 1745–1765.

——, V. O. Magaña, T. N. Palmer, J. Shukla, R. A. Tomas, M. Yanai, and T. Yasunari, 1998: Monsoons: Processes, predictability, and the prospects for prediction. *J. Geophys. Res.,* **103** (C7), 14 451–14 510.

Weickmann, K. M., 1983: Intraseasonal circulation and outgoing longwave radiation modes during Northern Hemisphere winter. *Mon. Wea. Rev.,* **111,** 1838–1858.

——, 1991: El-Niño/Southern Oscillation and Madden–Julian (30–60 Day) oscillations during 1981–1982. *J. Geophys. Res.,* **96,** 3187–3195.

——, and E. B. Berry, 2007: A synoptic–dynamic model of subseasonal atmospheric variability. *Mon. Wea. Rev.,* **135,** 449–474.

Wentz, F. J., C. Gentemann, D. Smith, and D. Chelton, 2000: Satellite measurements of sea surface temperature through clouds. *Science,* **288,** 847–850.

Wheeler, M. C., and G. N. Kiladis, 1999: Convectively coupled equatorial waves: Analysis of clouds and temperature in the wavenumber–frequency domain. *J. Atmos. Sci.,* **56,** 374–399.

——, and H. H. Hendon, 2004: An all-season real-time multivariate MJO index: Development of an index for monitoring and prediction. *Mon. Wea. Rev.,* **132,** 1917–1932.

——, and J. L. McBride, 2005: Australian–Indonesian monsoon. *Intraseasonal Variability of the Atmosphere–Ocean Climate System,* W. K. M. Lau and D. E. Waliser, Eds., Springer, 125–174.

Whitaker, J. S., and K. M. Weickmann, 2001: Subseasonal variations of tropical convection and week-2 prediction of wintertime western North American rainfall. *J. Climate,* **14,** 3279–3288.

Wong, S., and A. E. Dessler, 2007: Regulation of H2O and CO in tropical tropopause layer by the Madden–Julian oscillation. *J. Geophys. Res.,* **112,** D14305, doi:10.1029/2006JD007940.

Woodruff, S. D., H. F. Diaz, J. D. Elms, and S. J. Worley, 1998: COADS release 2 data and metadata enhancements for improvements of marine surface flux fields. *Phys. Chem. Earth,* **23,** 517–526.

Woolnough, S. J., J. M. Slingo, and B. J. Hoskins, 2000: The relationship between convection and sea surface temperature on intraseasonal time scales. *J. Climate,* **13,** 2086–2104.

——, F. Vitart, and M. A. Balmaseda, 2007: The role of the ocean in the Madden–Julian oscillation: Implications for MJO prediction. *Quart. J. Roy. Meteor. Soc.,* **133,** 117–128.

Xie, P. P., and P. A. Arkin, 1997: Global precipitation: A 17-year monthly analysis based on gauge observations, satellite estimates, and numerical model outputs. *Bull. Amer. Meteor. Soc.,* **78,** 2539–2558.

Yasunari, T., 1979: Cloudiness fluctuations associated with the Northern Hemisphere summer monsoon. *J. Meteor. Soc. Japan,* **57,** 227–242.

——, 1980: A quasi-stationary appearance of the 30–40 day period in the cloudiness fluctuations during the summer monsoon over India. *J. Meteor. Soc. Japan,* **58,** 225–229.

——, 1981: Structure of an Indian summer monsoon system with around 40-day period. *J. Meteor. Soc. Japan,* **59,** 336–354.

Yu, L., and R. A. Weller, 2007: Objectively analyzed air–sea heat fluxes for the global ice-free oceans (1981–2005). *Bull. Amer. Meteor. Soc.,* **88,** 527–539.

Zhang, C., 2005: Madden–Julian oscillation. *Rev. Geophys.,* **43,** RG2003, doi:10.1029/2004RG000158.

——, and J. Gottschalck, 2002: SST anomalies of ENSO and the Madden–Julian oscillation in the equatorial Pacific. *J. Climate,* **15,** 2429–2445.

——, H. H. Hendon, W. S. Kessler, and A. Rosati, 2001: Meeting summary: A workshop on the MJO and ENSO. *Bull. Amer. Meteor. Soc.,* **82,** 971–976.

——, M. Dong, S. Gualdi, H. H. Hendon, E. D. Maloney, A. Marshall, K. R. Sperber, and W. Q. Wang, 2006: Simulations of the Madden–Julian oscillation in four pairs of coupled and uncoupled global models. *Climate Dyn.,* **27,** 573–592, doi:10.1007/s00382-006-0148-2.

Zhang, Y., W. B. Rossow, A. A. Lacis, V. Oinas, and M. I. Mishchenko, 2004: Calculation of radiative fluxes from the surface to top of atmosphere based on ISCCP and other global data sets: Refinements of the radiative transfer model and the input data. *J. Geophys. Res.,* **109,** D19105, doi:10.1029/2003JD004457.

Zheng, Y., D. E. Waliser, W. F. Stern, and C. Jones, 2004: The role of coupled sea surface temperatures in the simulation of the tropical intraseasonal oscillation. *J. Climate,* **17,** 4109–4134.